The Astrophysical Journal, 903:140 (18pp), 2020 November 10 https://doi.org/10.3847/1538-4357/abbd94

Depletion of Bright Red Giants in the Galactic Center during Its Active Phases

Michal Zajaček[1], Anabella Araudo[2,3], Vladimír Karas[3], Bożena Czerny[1], and Andreas Eckart[4,5]
[1] Center for Theoretical Physics, Polish Academy of Sciences, Al. Lotnikow 32/46, 02-668 Warsaw, Poland; zajacek@cft.edu.pl
[2] ELI Beamlines, Institute of Physics, Czech Academy of Sciences, CZ-25241 Dolní Břežany, Czech Republic
[3] Astronomical Institute of the Czech Academy of Sciences, Boční II 1401, CZ-14100 Prague, Czech Republic
[4] I. Physikalisches Institut der Universität zu Köln, Zülpicher Strasse 77, D-50937 Köln, Germany
[5] Max-Planck-Institut für Radioastronomie (MPIfR), Auf dem Hügel 69, D-53121 Bonn, Germany
Received 2020 February 25; revised 2020 September 10; accepted 2020 September 29; published 2020 November 12

Abstract

Observations in the near-infrared domain showed the presence of the flat core of bright late-type stars inside ∼0.5 pc from the Galactic center supermassive black hole (Sgr A*), while young massive OB/Wolf–Rayet stars form a cusp. Several dynamical processes were proposed to explain this apparent paradox of the distribution of the Galactic center stellar populations. Given the mounting evidence on the significantly increased activity of Sgr A* during the past million years, we propose a scenario based on the interaction between the late-type giants and a nuclear jet, whose past existence and energetics can be inferred from the presence of γ-ray Fermi bubbles and bipolar radio bubbles. Extended, loose envelopes of red giant stars can be ablated by the jet with kinetic luminosity in the range of $L_{\rm j} \approx 10^{41}$–$10^{44}$ erg s^{-1} within the inner ∼0.04 pc of Sgr A* (S-cluster region), which would lead to their infrared luminosity decrease after several thousand jet–star interactions. The ablation of the atmospheres of red giants is complemented by the process of tidal stripping that operates at distances of $\lesssim$1 mpc, and by the direct mechanical interaction of stars with a clumpy disk at $\gtrsim$0.04 pc, which can explain the flat density profile of bright late-type stars inside the inner half parsec from Sgr A*.

Unified Astronomy Thesaurus concepts: Galactic center (565); Red giant stars (1372); Red supergiant stars (1375); Relativistic jets (1390); Stellar dynamics (1596)

1. Introduction

The Galactic center supermassive black hole (hereafter SMBH) with the mass of $4.1 \times 10^6 M_\odot$ is located at the distance of 8.1 kpc (Boehle et al. 2016; Gillessen et al. 2017; Parsa et al. 2017; Gravity Collaboration et al. 2018) and provides a unique laboratory for studying detailed dynamical processes and the mutual interaction between a nuclear star cluster (NSC) and a central massive black hole (Alexander 2005; Genzel et al. 2010; Eckart et al. 2017; Ali et al. 2020) as well as with the multiphase gaseous-dusty circumnuclear medium (Morris & Serabyn 1996; Różańska et al. 2017). The compact radio source Sgr A* associated with the SMBH is embedded in the Milky Way NSC, which is one of the densest stellar systems in the Galaxy (Alexander 2017; Schödel et al. 2014), and in addition, it is surrounded by an ionized, neutral, and molecular gas and dust (see, e.g., Moser et al. 2017 and references therein).

The NSC consists of both late-type (red giants, supergiants and asymptotic giant branch stars) and early-type stars of O and B spectral classes (Krabbe et al. 1991; Buchholz et al. 2009; Do et al. 2009; Gallego-Cano et al. 2018), which imply star formation during the whole Galactic history, albeit most likely episodic (Pfuhl et al. 2011; Schödel et al. 2020) with the star formation peak at 10 Gyr, the minimum at 1–2 Gyr, and a recent increase in the last few hundred million years.

In the innermost parsec of the Galactic center, there is a surprising abundance of young massive OB/Wolf–Rayet stars that have formed in situ in the last 10 million years (Ghez et al. 2003). These young stars form an unrelaxed cusp-like distribution. On the other hand, previous studies of the distribution of late-type stars showed that they exhibit a core-like distribution inside the inner ∼0.5 pc, which has a projected flat or even decreasing profile toward the center (Buchholz et al. 2009; Do et al. 2009; Sellgren et al. 1990). More recent studies provided a precise analysis of the distribution of late-type stars because of increasing their sensitivity toward larger magnitudes, i.e., fainter giants (Gallego-Cano et al. 2018; Habibi et al. 2019). Using photometric number counts and diffuse light analysis, Gallego-Cano et al. (2018) found that fainter late-type stars with magnitudes of $K \approx 18$ exhibit a cusp-like distribution within the sphere of influence of Sgr A* with a 3D power-law exponent of $\gamma \simeq 1.43$. In comparison, there is an apparent lack of bright red giants with $K = 12.5$–16 at the projected radii of $\lesssim$0.3 pc from Sgr A*. Gallego-Cano et al. (2018) estimate the number of missing giants to 100 for this distance range. The study of Habibi et al. (2019) also finds a cusp-like distribution for late-type stars with $K < 17$ within 0.02–0.4 pc. In agreement with Gallego-Cano et al. (2018), they found a core-like distribution for the brightest giants with $K < 15.5$, although the number of missing giants appears to be lower than 100 according to their analysis. Although the surface-brightness distribution of late-type stars brighter than 15.5 mag appears to be rather flat, already in Figure 11 of Buchholz et al. (2009) the inner point at $0\farcs5$ (where $1'' \sim 0.04$ pc at the Galactic center) of the distribution of late-type stars as well as of the distribution of all stars indicates the presence of a cusp.

In summary, there appears to be an internal mechanism within the NSC that preferentially depleted bright, large red giants on one hand, which has led to their apparent core-like distribution, and at the same time has been less efficient for early-type as well as fainter late-type stars, on the other hand. Such a mechanism has altered either the spatial, luminosity, or the temperature distribution of the bright red giant stars so that they effectively fall beyond the detection limit or they instead mimic younger, "bluer" stars. So far, it is mainly the following four mechanisms that have been discussed to explain the apparent lack of bright red giants:

1. complete or partial tidal disruption of red giants by the SMBH (Hills 1975; Bogdanović et al. 2014; King 2020; envelope removal),
2. envelope stripping by the collisions of red giants with the dense clumps within a self-gravitating accretion disk (Armitage et al. 1996; Amaro-Seoane & Chen 2014; Kieffer & Bogdanović 2016; Amaro-Seoane et al. 2020; envelope removal),
3. collisions of red giants with field stars and compact remnants (Phinney 1989; Morris 1993; Genzel et al. 1996; Bailey & Davies 1999; Alexander 2005; Davies & King 2005; Dale et al. 2009; envelope removal),
4. mass segregation effects: the dynamical effect of a secondary massive black hole (Baumgardt et al. 2006; Merritt & Szell 2006; Portegies Zwart et al. 2006; Matsubayashi et al. 2007; Löckmann & Baumgardt 2008; Gualandris & Merritt 2012) or of an infalling massive cluster (Kim & Morris 2003; Ernst et al. 2009; Antonini et al. 2012) or of stellar black holes (Morris 1993; altered spatial distribution),

where in parentheses we include the mechanism responsible for altering the population of late-type stars. The importance of star–star and star–disk interactions was also analyzed generally for active galactic nuclei (AGNs) in terms of the effects on the accretion disk and broad-line region structure as well as the NSC orbital distribution (Zurek et al. 1994; Armitage et al. 1996; Karas & Šubr 2001; Vilkoviskij & Czerny 2002; Kieffer & Bogdanović, 2016; MacLeod & Lin 2020).

We propose here another mechanism based on the jet–star interactions (Barkov et al. 2012a; Araudo et al. 2013; Araudo & Karas 2017), which most likely coexisted with the mechanisms proposed above. In particular, the star–accretion disk collisions are expected to be accompanied by star–jet crossings during previous active phases of Sgr A*. Because red giant stars have typically large, loosely bound tenuous envelopes, dense compact cores, and slow winds with the terminal velocity $\lesssim$100 km s^{-1}, they are in particular susceptible to mass removal in encounters with higher-pressure material (MacLeod et al. 2012; Amaro-Seoane & Chen 2014; Kieffer & Bogdanović 2016).[6] Therefore, during the red giant–jet interactions, the jet ram pressure will remove the outer layers of the stellar envelope during the passage. We illustrate this idea in Figure 1.

After several star–jet crossings, the atmosphere is removed similarly as for repetitive star–disk crossings (Amaro-Seoane et al. 2020), and the giant is modified in a way that it follows an evolutionary track in the Hertzsprung–Russell (HR) diagram approximately along the constant absolute magnitude toward higher effective temperatures. We show that this mechanism quite likely operated in the vicinity of Sgr A* during its active Seyfert-like phase in the past few million years (Bland-Hawthorn et al. 2019) when the jet kinetic luminosity could have reached $\sim 10^{44}$ erg s^{-1}. In principle, even in the quiescent state, a tidal disruption event (TDE) every $\sim 10^4$ yr, which can be estimated for the Galactic center (Syer & Ulmer 1999; Alexander 2005), can temporarily reactivate the jet of Sgr A*, and some of the bright red giants could be depleted during its existence. This makes the red giant–jet interaction in the

[6] The estimate of the terminal wind velocity is given by the escape velocity $v_{\rm esc} = 62\left(\frac{M_\star}{1\,M_\odot}\right)^{1/2}\left(\frac{R_\star}{100\,R_\odot}\right)^{-1/2}$ km s^{-1}.

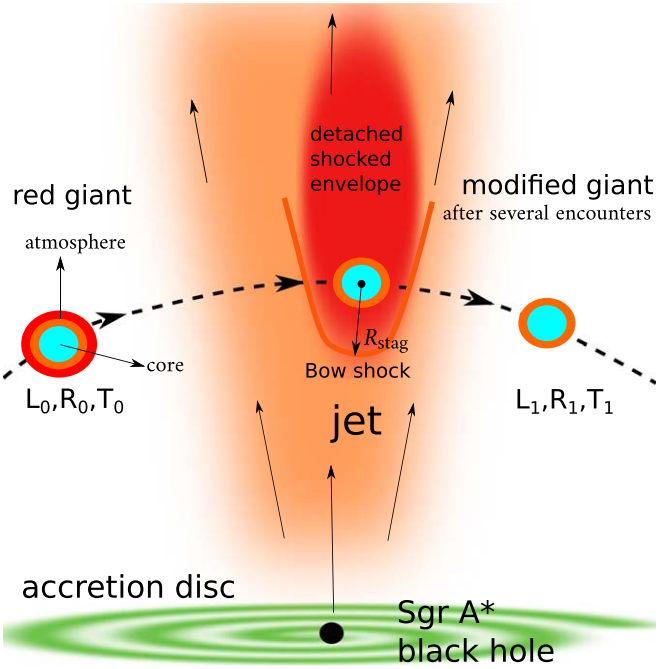

Figure 1. Illustration of the jet–red giant interaction in the vicinity of Sgr A* during its active phase. The large, loosely bound envelope of the red giant (colored as red and orange), which has an initial luminosity, radius, and temperature (L_0, R_0, T_0), is ablated by the jet ram pressure during several encounters as the lifetime of the jet $t_{\rm jet} \sim 0.5$ Myr is much longer than the orbital timescale in the inner $\sim$0.5 pc, $P_{\rm orb} \sim 1500(a/0.1\ {\rm pc})^{3/2}$ yr. After a few hundred encounters, star has modified parameters (L_1, R_1, T_1), which change the overall outlook of the giant in the near-infrared domain. Inspired by Barkov et al. (2012a) and Bosch-Ramon et al. (2012).

Galactic center relevant and highly plausible in its recent history, and the dynamical consequences can be inferred based on the so-far detected traces of the past active phase of Sgr A* as well as the currently observed stellar density distribution.

Previous jet–star interaction studies were focused on the emergent nonthermal radiation, in particular in the gamma-ray domain, and mass-loading and chemical enrichment of jets by stellar winds (see e.g., Komissarov 1994; Barkov et al. 2012a; Bosch-Ramon et al. 2012; Araudo et al. 2013; Bednarek & Banasiński 2015; de la Cita et al. 2016). Here we focus on the effect of the jet on the stellar population. In most jetted AGNs, this is perhaps a secondary problem because stellar populations in the host bulge cannot be resolved out, i.e., one can only analyze the integrated starlight. In contrast, within the Galactic center NSC, one can not only disentangle late- and early-type stars, but it is also possible to study their distribution as well as the kinematics of individual stars. Although in the current low-luminosity state there is no firm evidence for the presence of a relativistic jet, there are nowadays several multiwavelength signatures of the past active Seyfert-like state of Sgr A* that occurred a few million years ago (Bland-Hawthorn et al. 2019; Heywood et al. 2019; Ponti et al. 2019). However, even in the current quiescent state of Sgr A*, studies by Yusef-Zadeh et al. (2012) and Li et al. (2013) indicate the existence of a low-surface-brightness parsec-scale jet. In addition, the presence of the cometary-shaped infrared-excess bow-shock sources X3, X7 (Mužić et al. 2010), and recently X8 (Peißker et al. 2019) indicates that the star–outflow interaction is ongoing even in a very low state of the Sgr A* activity. The morphology of these sources can be explained by the interaction with a strong

accretion wind originating from Sgr A* or with the collective wind of the cluster of young stars.

This paper proposes a new mechanism that could have affected the current population of bright late-type stars, namely their appearance as well as number counts in specific magnitude bins, in the Galactic center. We apply analytical and semianalytical calculations to assess whether the potential past jet–star interactions could have had an effect on the stellar population in the sphere of influence of Sgr A*. Although the analytical calculations introduce several simplifications, we show that the mechanism could have operated and the estimated number of affected red giants is in accordance with the most sensitive, up-to-date studies (Gallego-Cano et al. 2018; Habibi et al. 2019). A more detailed computational treatment including magnetohydrodynamic numerical simulations as well as a stellar evolution will be presented in our future studies.

The paper is structured as follows. In Section 2, we derive the stagnation radius, basic timescales, and the envelope mass removed for red giant stars interacting with the jet of Sgr A* during its past active phase. In Section 3, we discuss the observational signatures in the near-infrared domain. Subsequently, in Section 4, we estimate the number of red giants that could be affected by the jet interaction and visually depleted from the immediate vicinity of Sgr A*. In Section 6, we discuss additional processes related to the red giant–jet interaction in the Galactic center. Finally, we summarize the main results and conclude with Section 7.

2. Derivation of the Jet–Star Stagnation Radius and the Jet-induced Stellar Mass Loss

The evidence for the active phase of Sgr A* that is estimated to have occurred 4 ± 1 Myr ago is based on the X-ray/γ-ray bubbles with a total energy content of 10^{56}–10^{57} erg (Bland-Hawthorn et al. 2019). The first evidence for the nuclear outburst was the kiloparsec-scale 1.5 keV ROSAT X-ray emission that originated in the Galactic center (Bland-Hawthorn & Cohen 2003). The X-ray structure coincides well with the more recently discovered Fermi γ-ray bubbles extending 50° north and south of the Galactic plane at 1–100 GeV (Su et al. 2010). The X-ray/γ-ray bubbles are energetically consistent with the nuclear AGN-like activity associated with the jet and/or disk-wind outflows with jet power $L_{\rm j} = 2.3^{+5.1}_{-0.9} \times 10^{42}$ erg s^{-1} and age $4.3^{+0.8}_{-1.4}$ Myr (Miller & Bregman 2016). In comparison, the starburst origin of the Fermi bubbles is inconsistent with the bubble energetics by a factor of ∼100 (Bland-Hawthorn & Cohen 2003). On intermediate scales of hundreds of parsecs, the base of the Fermi bubbles coincides with the bipolar radio bubbles (Heywood et al. 2019) as well as with the X-ray chimneys (Ponti et al. 2019).

Using hydrodynamic simulations, Guo & Mathews (2012) reproduce the basic radiative characteristics of the Fermi bubbles with the AGN jet duration of ∼0.1–0.5 Myr, which corresponds to the jet luminosity $L_{\rm j} \approx 10^{56-57}\,{\rm erg}/(0.1-0.5\,{\rm Myr}) = 6.3 \times 10^{42} - 3.2 \times 10^{44}$ erg s^{-1}. The jet is dominated by the kinetic luminosity $L_{\rm j} = \eta_{\rm j} L_{\rm acc}$, where $\eta_{\rm j}$ is the conversion efficiency from the accretion luminosity $L_{\rm acc}$ to the jet kinetic luminosity. The accretion luminosity is $L_{\rm acc} \lesssim L_{\rm Edd}$, where the Eddington luminosity is

$$L_{\rm Edd} = 5.03 \times 10^{44} \left(\frac{M_\bullet}{4 \times 10^6\, M_\odot} \right) {\rm erg\ s^{-1}}, \quad (1)$$

and $\eta_{\rm j} < 0.7$ for most radio sources (Ito et al. 2008). This yields the maximum jet kinetic luminosity for Sgr A* of $L_{\rm j} \approx 3.5 \times 10^{44}$ erg s^{-1}. We will consider $L_{\rm j} \approx 10^{41} - 10^{44}$ erg s^{-1}, where the lower limit is given by the putative jet present in the current quiescent state (Yusef-Zadeh et al. 2012), with the inferred kinetic luminosity of $L_{\rm min} \sim 1.2 \times 10^{41}$ erg s^{-1}, and the upper limit is given by the Eddington luminosity.

We assume a conical jet with a half-opening angle θ and width $R_{\rm j} = z \tan\theta$, where z is the distance to Sgr A*. The jet footpoint for Sgr A* can be estimated to be located at $z_0 \sim 2 \times 10^{-5} (M_\bullet/4 \times 10^6\, M_\odot)\,{\rm pc} = 52 R_{\rm Schw}$ (Junor et al. 1999), where $R_{\rm Schw} = 2GM_\bullet/c^2 = 3.8 \times 10^{-7} (M_\bullet/4 \times 10^6\, M_\odot)$ pc is the Schwarzschild radius. Any red giant or supergiant with radius[7] $R_\star$ and mass $m_\star$ is not expected to plunge below z_0 as the tidal disruption radius $r_{\rm t} = R_\star (2M_\bullet/m_\star)^{1/3}$ (Hills 1975; Rees 1988) is at least a factor of 2 larger,

$$\frac{r_{\rm t}}{R_{\rm Schw}} = 1\,20 \left(\frac{R_\star}{10\, R_\odot} \right) \left(\frac{M_\bullet}{4 \times 10^6\, M_\odot} \right)^{\frac{1}{3}} \left(\frac{m_\star}{M_\odot} \right)^{-\frac{1}{3}}. \quad (2)$$

$R_\star = 10\, R_\odot$ and $m_\star = 1\, M_\odot$ are typical intermediate values for the evolved late-type giants with extended envelopes (Merritt 2013). For numerical estimates, we consider the range of radii for red giants and supergiants, $R_\star \sim$ 4–1000 $R_\odot$, as indicated by the HR diagram. These late-type stars have a large range of bolometric luminosities, $L_\star \sim$ 10–72,000$L_\odot$, and the temperature range of $T_\star \sim$ 5000–3000 K, which corresponds to the spectral classes K and M, respectively. The K-band magnitude range is $K \sim 15.2$ mag for $R_\star = 4\, R_\odot$, $T_\star = 5000$ K, and $K \sim 4.4$ mag for $R_\star = 1000\, R_\star$, $T_\star = 3000$ K. More specifically, we focus on late-type stars of $K = 16$ mag and brighter, which appear to form a core-like density distribution in the central 0.5 pc. Using the isochrones obtained with the Parsec code (Bressan et al. 2012), these stars have $R_\star \sim 4\, R_\odot$ and larger for an age of 5 Gyr. The late-type stars that are completely absent in the S cluster (inner ∼0.04 pc) were inferred to have $R_\star = 30\, R_\odot$ and larger (Habibi et al. 2019). Therefore, numerical estimates are typically scaled to $R_\star = 30\, R_\odot$ unless otherwise indicated.

We will further focus on the region between the tidal radius of red giants and the outer edge of the S cluster, which approximately corresponds to the Bondi radius of the hot bremsstrahlung plasma (Baganoff et al. 2003; Wang et al. 2013),

$$R_{\rm B} = \frac{GM_\bullet}{c_{\rm s}^2} = 0.12 \left(\frac{M_\bullet}{4 \times 10^6\, M_\odot} \right) \left(\frac{T_{\rm p}}{10^7\ {\rm K}} \right)^{-1} {\rm pc}, \quad (3)$$

which is two to three orders of magnitude larger than the tidal radius of red giants, $R_{\rm B} \sim 3.1 \times 10^5\, R_{\rm Schw}$. More generally speaking, the population of predominantly B-type stars lies within the innermost arcsecond (∼0.04 pc, S cluster), while the population of young massive OB/Wolf–Rayet stars stretches from ∼0.04 pc up to ∼0.5 pc, a fraction of which forms a warped stellar disk (Genzel et al. 2010).

The stellar-wind ram pressure at a distance r from the center of the star can be estimated as $P_{\rm sw} \sim \rho_{\rm w} v_{\rm w}^2 = \dot{m}_{\rm w} v_{\rm w}/(4\pi r^2)$,

[7] The stellar radius is the sum of the core radius and the envelope radius, $R_\star = R_{\rm c} + R_{\rm env}$.

where $\dot{m}_{\rm w}$ is the mass-loss rate and $v_{\rm w}$ is the terminal wind velocity. Using typical values for red giants with $\dot{m}_{\rm w} \approx 10^{-8}\,M_\odot\ {\rm yr}^{-1}$ and $v_{\rm w} \approx 10\ {\rm km\ s}^{-1}$ (e.g., Reimers 1987; de la Cita et al. 2016),[8]

$$P_{\rm sw} = 0.012\left(\frac{\dot{m}_{\rm w}}{10^{-8}\,M_\odot\ {\rm yr}^{-1}}\right)\left(\frac{v_{\rm w}}{10\ {\rm km\ s}^{-1}}\right) \times \left(\frac{r}{30\,R_\odot}\right)^{-2}\ {\rm erg\ cm}^{-3}. \quad (4)$$

The ram pressure of a relativistic jet with bulk motion Lorentz factor Γ is $P_{\rm j} = \Gamma\rho_{\rm j}v_{\rm j}^2$, where the jet density is $\rho_{\rm j} = L_{\rm j}/[(\Gamma-1)c^2\sigma_{\rm j}v_{\rm j}]$ and $\sigma_{\rm j} = \pi R_{\rm j}^2$ is the jet cross-sectional area. By assuming $v_{\rm j} \sim c$ and $\Gamma \sim 10$, the jet kinetic pressure for Sgr A* can be written as

$$P_{\rm j} \approx \frac{L_{\rm j}}{\sigma_{\rm j}c} = \frac{L_{\rm j}}{\pi c z^2\tan^2\theta} = 0.014\left(\frac{L_{\rm j}}{10^{42}\ {\rm erg\ s}^{-1}}\right)\left(\frac{z}{0.04\ {\rm pc}}\right)^{-2}\ {\rm erg\ cm}^{-3}, \quad (5)$$

where we have assumed $\theta \simeq 12.^\circ5$, which corresponds to the jet sheath half-opening angle estimated for the current candidate jet of Sgr A* (Li et al. 2013). Note that the innermost arcsecond ($z \sim 0.04$ pc) is also the outer radius of fast-moving stars in the S cluster (Genzel et al. 2010; Eckart et al. 2017).

By equating $P_{\rm sw} = P_{\rm j}$, we obtain the stagnation distance

$$\frac{R_{\rm stag}}{R_\odot} = 27\left(\frac{z}{0.04\ {\rm pc}}\right)\left(\frac{\dot{m}_{\rm w}}{10^{-8}\,M_\odot{\rm yr}^{-1}}\right)^{\frac{1}{2}} \times \left(\frac{v_{\rm w}}{10\ {\rm km\ s}^{-1}}\right)^{\frac{1}{2}}\left(\frac{L_{\rm j}}{10^{42}\ {\rm erg\ s}^{-1}}\right)^{-\frac{1}{2}}, \quad (6)$$

which characterizes by how much the red giant envelope can be ablated by the jet in one encounter. Note that $R_{\rm stag} < R_\star$ for late-type giants and supergiants with $R_\star \sim 100$–$1000\,R_\odot$ (see Figure 2). The very tenuous wind of red giants cannot balance the jet ram pressure, and therefore, the jet plasma impacts on the stellar surface. As a consequence, a fraction of the stellar envelope is removed as estimated by Equation (6).

Interestingly, giant stars with $R_\star \gtrsim 30\,R_\odot$ appear to be missing in the S cluster. Only late-type stars with $R_\star$ between 4 and $30\,R_\odot$ (with absolute bolometric magnitudes between -1.05 and 3.32, respectively, for the effective temperature of 4000 K) were detected by Habibi et al. (2019; see their Figure 2). Stars with $4 \leqslant R_\star/R_\odot \leqslant 30$ within 0.02 pc have $R_{\rm stag}/R_\star \sim 1$ when $2\times10^{41} \leqslant L_{\rm j}/{\rm erg\ s}^{-1} \leqslant 1.1\times10^{43}$, as indicated in Figure 2. This is in agreement with the estimated jet power $L_{\rm j} \sim 2.3\times10^{42}\ {\rm erg\ s}^{-1}$ from X- and γ-ray bubbles (Miller & Bregman 2016). Therefore, an apparent lack of late-type giant stars with envelopes $R_\star \gtrsim 30\,R_\odot$ in the inner $\sim$0.04 pc of Galactic center could result from the jet-induced ablation of the stellar envelope during the last active phase of Sgr A*, a few million years ago.

[8] For red giants, $\dot{m}_{\rm w} \approx 10^{-6}$–$10^{-9}\,M_\odot\ {\rm yr}^{-1}$ according to Reimers (1987).

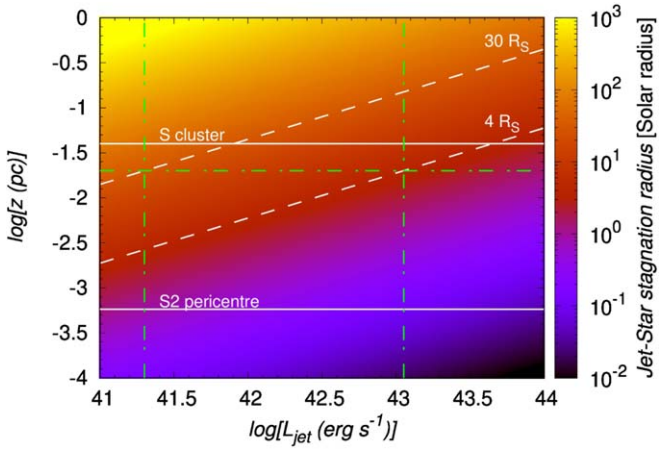

Figure 2. Stagnation radius $R_{\rm stag}/R_\odot$. The two horizontal white solid lines indicate the radial extent of the S cluster between the S2 pericenter distance and the outer radius at $\sim$0.04 pc. The two white dashed lines stand for the atmosphere radius limits of late-type stars in the S cluster, $4R_\odot$ and $30R_\odot$ (Habibi et al. 2019). The dotted–dashed green lines indicate the jet luminosity limits that would yield the stellar atmosphere ablation at 30 and $4R_\odot$ at $z = 0.02$ pc.

2.1. Basic Timescales of the Jet–Star Interaction

The red giant will enter the jet and not mix with its sheath layers on the surface if $v_{\rm orb} \gtrsim v_{\rm sc}$, where $v_{\rm orb} \sim (GM_\bullet/z)^{1/2}$ is the Keplerian orbital velocity of the star around Sgr A* and $v_{\rm sc} \sim c(\Gamma\rho_{\rm j}/\rho_\star)$ is the sound speed inside the shocked obstacle. This condition can be written as

$$\frac{\rho_\star}{\rho_{\rm j}} \gtrsim 5.2\times10^5\left(\frac{z}{0.01\ {\rm pc}}\right)\left(\frac{\Gamma}{10}\right)\left(\frac{M_\bullet}{4\times10^6\,M_\odot}\right)^{-1}, \quad (7)$$

which means that stellar atmosphere layers of comparable density or greater than indicated by Equation (7) will enter the jet, and the less dense upper layers will mix with the jet surface layers.

Once inside, the bow shock is formed inside the jet on the very short timescale of $t_{\rm bs} \sim R_\star/c \sim 232(R_\star/100\,R_\odot)$s. A shock also propagates through the red-giant atmosphere on the shock-crossing or dynamical timescale, $t_{\rm d} \sim R_\star/v_{\rm sc}$, whose lower limit is imposed by the condition of penetration, $v_{\rm orb} \gtrsim v_{\rm sc}$, which leads to $t_{\rm d} \gtrsim R_\star/v_{\rm orb} = R_\star\sqrt{z/(GM_\bullet)} \sim 53063(R_\star/100\,R_\odot)(z/0.01\ {\rm pc})^{1/2}(M_\bullet/4\times10^6\,M_\odot)^{-1/2}$ s. The dynamical, shock-crossing time is at least $\sim$10 times longer than the bow-shock formation time close to the footpoint of the jet, but the ratio becomes larger with the distance from Sgr A* as $t_{\rm d}/t_{\rm bs} \gtrsim 229(z/0.01\ {\rm pc})^{1/2}(M_\bullet/4\times10^6)^{-1/2}$.

The star-crossing time through the jet can be estimated as $t_\star \sim 2R_{\rm j}/v_{\rm orb}$. Using $R_{\rm j} = z\tan\theta$ and the condition $v_{\rm sc} \lesssim v_{\rm orb}$, we obtain

$$\frac{t_\star}{t_{\rm d}} \lesssim \frac{2z\tan\theta}{R_\star} \sim 1966, \quad (8)$$

which implies that the shock propagates throughout the detached envelope, which is dragged by the jet and mixed with its material. Eventually, after several $t_{\rm d}$, the envelope material will reach the velocity of $v_{\rm j} \sim c$. Note that $t_\star/t_{\rm d} \sim 1$ when $z \sim 10^{-5}$ pc; hence, the removed envelope material should be dragged by the jet throughout the whole NSC.

The ablated red giant after the first crossing through the jet would first expand adiabatically to the original size on the

thermal expansion timescale $t_{\rm exp} \sim R_\star/c_{\rm s} = R_\star\sqrt{\mu m_{\rm H}/(k_{\rm B}T_{\rm atm})} = 0.2(R_\star/100\,R_\odot)(T_{\rm atm}/10^4\,{\rm K})^{-1/2}$ yr because of the pressure of the warmer, underlying layers as the star adjusts its size to reach a hydrodynamic equilibrium. This expansion timescale is shorter than the orbital timescale

$$P_{\rm orb} = 2\pi\left(\frac{z^3}{GM_\bullet}\right)^{1/2} = 47\left(\frac{z}{0.01\ {\rm pc}}\right)^{3/2}\left(\frac{M_\bullet}{4\times10^6\,M_\odot}\right)^{-1/2}\ {\rm yr}. \quad (9)$$

Kieffer & Bogdanović (2016) infer a similar timescale for the envelope expansion using the hydrodynamic simulations of red giant–accretion-clump collisions. According to their Figure 7, the envelope expands to a larger size than the original stellar radius in $t_{\rm exp} \sim 1.5t_{\rm dyn}$ after the star emerges from the accretion clump, where $t_{\rm dyn}$ is a dynamical timescale of the star,

$$t_{\rm dyn} \sim 0.32\left(\frac{R_\star}{100\,R_\odot}\right)^{3/2}\left(\frac{m_\star}{1\,M_\odot}\right)^{-1/2}\ {\rm yr}, \quad (10)$$

which leads to $t_{\rm exp} \sim 1.5 \times 0.32$ yr ≈ 0.5 yr.

The timescale of the thermal evolution of a star after the jet–star interaction is expressed by the Kelvin–Helmholtz (KH) or thermal timescale,

$$t_{\rm KH} \approx \frac{Gm_\star^2}{R_\star L_\star} = 210\left(\frac{m_\star}{1\,M_\odot}\right)^2\left(\frac{R_\star}{100\,R_\odot}\right)^{-1}\left(\frac{L_\star}{1500L_\odot}\right)^{-1}\ {\rm yr}, \quad (11)$$

where we estimated the stellar luminosity using $L_\star = 4\pi R_\star^2\sigma T_\star^4$ for $T_\star = 3500$–3700 K typical of red giants. For the whole range of stellar radii $R_\star \sim 4$–$1000\,R_\odot$ and stellar luminosities $L_\star \sim 10$–$7.2\times10^3\,L_\odot$, $t_{\rm KH}$ differs considerably —from $\sim10^6$ yr for the smallest giants to ~0.43 yr for the largest ones.

Based on the comparison between the time between jet–star collisions $t_{\rm c} = P_{\rm orb}/2$ and the KH timescale, one can distinguish cool colliders when $t_{\rm c} \gtrsim t_{\rm KH}$, i.e., the star had enough time to radiate away the accumulated collisional heat, and it cools down and shrinks before the next collision. For the case when $t_{\rm c} < t_{\rm KH}$, there is not enough time to radiate away the excess collisional heat, and the star is warmer and larger at the time of the subsequent collision—these are the so-called warm colliders. In the nuclear star cluster when the jet was active, there were both types of colliders with the approximate division given by $t_{\rm c} \approx t_{\rm KH}$, which leads to

$$z_{\rm c} \approx \frac{Gm_\star^{4/3}M_\bullet^{1/3}}{R_\star^{2/3}L_\star^{2/3}\pi^{2/3}} = 0.04\left(\frac{m_\star}{1\,M_\odot}\right)^{4/3}\left(\frac{M_\bullet}{4\times10^6\,M_\odot}\right)^{1/3} \times\left(\frac{R_\star}{100\,R_\odot}\right)^{-2/3}\left(\frac{L_\star}{1500L_\odot}\right)^{-2/3}\ {\rm pc}. \quad (12)$$

The length scale $z_{\rm c}$ implies that red giants located inside the inner S cluster were collisionally heated up and bloated, which increased their mass removal during repetitive encounters with the jet. Stars orbiting at larger distances managed to cool down and shrink in size before the next collision, which has subsequently diminished their overall mass loss. However, note that Equation (12) is a function of the stellar parameters $m_\star$, $R_\star$, and $L_\star$, hence $z_{\rm c}$ differs depending on the red giant stage and its mass. For the smallest late-type stars with $R_\star \sim 4\,R_\odot$ and $L_\odot \sim 8.9\,L_\odot$, $z_{\rm c} \sim 10.5$ pc; therefore, they can be classified as warm colliders throughout the nuclear star cluster. On the other hand, the late-type supergiants with $R_\star \sim 10^3\,R_\odot$ and $L_\odot \sim 7.2\times10^4\,L_\odot$ have $z_{\rm c} \sim 0.7$ mpc, hence they can be classified as cool colliders beyond milliparsec distances.

2.2. Jet-induced Envelope Removal

The stellar evolution after a jet–star encounter is generally complicated given that the envelopes of red giants become bloated after the first passage through the jet. This is because of the pressure of lower, hotter layers and their subsequent nearly adiabatic expansion, which can make the red giant even larger and brighter (Kieffer & Bogdanović 2016). Note that the number of encounters $n_{\rm cross} = 2t_{\rm jet}/P_{\rm orb}$, where $t_{\rm jet} \sim 0.5$ Myr is the jet lifetime, is typically $\gg1$. In particular,

$$n_{\rm cross} \sim 2\times10^4\left(\frac{t_{\rm jet}}{0.5\ {\rm Myr}}\right)\left(\frac{M_\bullet}{4\times10^6\,M_\odot}\right)^{\frac{1}{2}}\left(\frac{z}{0.01\ {\rm pc}}\right)^{-\frac{3}{2}}. \quad (13)$$

The number of encounters is also at least two orders of magnitude larger than the one expected from the star–accretion-clump interaction investigated by Kieffer & Bogdanović (2016) and Amaro-Seoane et al. (2020). After the first passage, the bloated red giant has an even larger cross section than before the encounter, which increases the mass removed during subsequent encounters (Armitage et al. 1996; Kieffer & Bogdanović 2016). The jet–star interaction phase proceeds during the red giant lifetime, which is $t_{\rm rg} \sim 10^8$ yr (MacLeod et al. 2012). During the red giant phase, there are $n_{\rm orb} = t_{\rm rg}/P_{\rm orb} \sim 2.1\times10^6(z/0.01\ {\rm pc})^{-3/2}$ orbits around Sgr A*, out of which $n_{\rm cross}/n_{\rm orb} = 2t_{\rm jet}/t_{\rm rg} \sim 1\%$ involve the interaction with the jet, assuming there was only one period of increased activity of Sgr A* in the last 100 million years. This ensures that the repetitive jet–red giant interaction leads to substantial mass loss, and the upper layer of the envelope is eventually removed.

The mass removal in a single passage due to atmosphere ablation ΔM_1 can be estimated through the balance of the jet ram force and the gravitational force acting on the envelope, i.e., $P_{\rm j}\pi R_\star^2 \simeq G\Delta M_1 m_\star/R_\star^2$, giving (Barkov et al. 2012a)

$$\frac{\Delta M_1^{\rm max}}{M_\odot} \approx 4\times10^{-10}\left(\frac{L_{\rm j}}{10^{42}\ {\rm erg\ s^{-1}}}\right)\left(\frac{R_\star}{100\,R_\odot}\right)^4 \times\left(\frac{z}{0.04\ {\rm pc}}\right)^{-2}\left(\frac{\theta}{0.22}\right)^{-2}\left(\frac{m_\star}{M_\odot}\right)^{-1}. \quad (14)$$

In Figure 3, we plot ΔM_1. Note that $\Delta M_1 \ll m_\star$ and, therefore, the orbital dynamics is not significantly affected by a single passage through the jet. However, given that $\Delta M_1 \propto R_\star^4 z^{-2}$, the mass loss can be about one-thousandth to one-hundredth of the mass of a star for the largest giants on the asymptotic giant branch with $R_\star \sim 10^3\,R_\odot$ and distances an order of magnitude smaller than $z \simeq 0.04$ pc (see the yellowish region in Figure 3). In fact, the

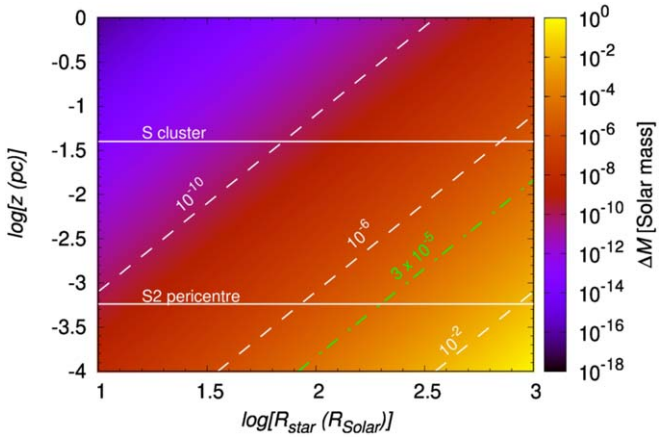

Figure 3. Mass removed from the red giant envelope for a single jet–star interaction, ΔM in Equation (14), for the case with $L_{\rm j} = 10^{42}$ erg s^{-1}, $m_\star = 1\,M_\odot$, and $\theta = 12.^\circ5$. The two horizontal lines indicate the radial extent of the S cluster between the S2 pericenter distance and the outer radius at $z \sim 0.04$ pc. Dashed lines indicate $\Delta M/M_\odot = 10^{-10}$, 10^{-6}, and 10^{-2}. The dotted–dashed green line corresponds to $\Delta M = 3 \times 10^{-5} M_\odot$, which is equivalent to $\Delta M = 6 \times 10^{28}$ g in Equation (6) of Barkov et al. (2012a).

value of $\Delta M_{\rm l} = 6 \times 10^{28}\,{\rm g} = 3 \times 10^{-5}\,M_\odot$ discussed by Barkov et al. (2012a) for powerful blazars in connection to their very high-energy γ-ray emission can be reached in the Galactic center for red giants with radii $R_\star > 200\,R_\odot$ at $z < 0.01$ pc. Such a large mass-loss with a certain momentum with respect to the star can already have an effect on the orbital dynamics, taking into account repetitive encounters of the red giant with the jet. In other words, the mass removal takes place at the expanse of the kinetic energy of the star, which has implications for the dynamics of the NSC; see also Kieffer & Bogdanović (2016) for discussion. In addition, already for jets with a lower power corresponding to the active phase of the Galactic center, jet–red giant interactions can affect the short-term TeV emission in these sources. These effects are beyond the scope of the current paper and will be investigated in our future studies.

The mass removal during a single jet encounter given by Equation (14) can be considered as an upper limit as we assume that the cross section of the star is given by its radius during the entire passage of the star through the jet, hence $\Delta M_{\rm l}^{\rm max} \approx P_{\rm j}\pi R_\star^4/(Gm_\star)$. However, this is only an approximation as realistically, during a few shock-crossing or dynamical timescales $t_{\rm d}$, the ram pressure of the jet will shape the red giant and its detached envelope into a comet-like structure (see Figure 1) for which the interaction cross section is given by $R_{\rm stag}$ rather than by $R_\star$, which gives us a lower limit on the mass removal, $\Delta M_{\rm l}^{\rm min} \approx P_{\rm j}\pi R_{\rm stag}^4/(Gm_\star) \leqslant \Delta M_{\rm l}^{\rm max}$. Using Equation (6), $\Delta M_{\rm l}^{\rm min}$ can be expressed in terms of the basic parameters of the star and the jet, and it can numerically be expressed by the same units as in Equations (14) and (6),

$$\frac{\Delta M_{\rm l}^{\rm min}}{M_\odot} \approx \frac{c(\dot m_{\rm w} v_{\rm w} z \tan\theta)^2}{16 G m_\star L_{\rm j}} = 2.1 \times 10^{-12}\left(\frac{L_{\rm j}}{10^{42}\,{\rm erg\,s^{-1}}}\right)^{-1}\left(\frac{m_\star}{M_\odot}\right)^{-1} \times \left(\frac{\dot m_{\rm w}}{10^{-8}\,M_\odot\,{\rm yr^{-1}}}\right)^2\left(\frac{v_{\rm w}}{10\,{\rm km\,s^{-1}}}\right)^2\left(\frac{z}{0.04\,{\rm pc}}\right)^2, \quad (15)$$

where we adopted $\theta \sim 12.^\circ5$ as before. In comparison with $\Delta M_{\rm l}^{\rm max}$ in Equation (14), which is proportional to z^{-2}, $\Delta M_{\rm l}^{\rm min}$ in Equation (15) increases as z^2. This implies that $\Delta M_{\rm l}^{\rm min} \leqslant \Delta M_{\rm l}^{\rm max}$ holds for $z \leqslant z_{\rm stag}$, where at $z_{\rm stag}$, $R_\star = R_{\rm stag}$. In other words, only at $z < z_{\rm stag}$ is the mass removal due to the jet activity from the red giant atmosphere possible, while at distances larger than $z_{\rm stag}$, the jet ablation is limited to the stellar-wind material, as is the case for the observed comet-shaped sources X3, X7, and X8 (Mužić et al. 2010; Peißker et al. 2019). From Equation (6), the relation for $z_{\rm stag}$ follows as

$$z_{\rm stag} \approx 0.15\left(\frac{R_\star}{100\,R_\odot}\right)\left(\frac{\theta}{0.22}\right)^{-1}\left(\frac{L_{\rm j}}{10^{42}\,{\rm erg\,s^{-1}}}\right)^{\frac{1}{2}} \times \left(\frac{\dot m_{\rm w}}{10^{-8}\,M_\odot\,{\rm yr^{-1}}}\right)^{-\frac{1}{2}}\left(\frac{v_{\rm w}}{10\,{\rm km\,s^{-1}}}\right)^{-\frac{1}{2}}{\rm pc}. \quad (16)$$

The dependence of $z_{\rm stag}$ on the stellar radius and the mass-loss rate is shown in Figure 4 (left panel). It is apparent that the volume around the reactivated Sgr A*, where the jet ablation can occur for a particular red giant, depends considerably on $\dot m_{\rm w}$, which spans over three orders of magnitude depending on the evolutionary stage, $\dot m_{\rm w} \approx 10^{-9} - 10^{-6}\,M_\odot\,{\rm yr^{-1}}$ (Reimers 1987). In particular, for red giants with $R_\star = 10\,R_\odot$, $z_{\rm stag}$ shrinks from 0.047 pc to 0.0015 pc as the mass-loss rate increases from $\dot m_{\rm w} = 10^{-9}\,M_\odot\,{\rm yr^{-1}}$ to $10^{-6}\,M_\odot\,{\rm yr^{-1}}$.

In Figure 4 (right panel), we show an exemplary case for the mass removal range from the red giant atmosphere (red giant with the parameters of $R_\star = 100\,R_\odot$, $\dot m_{\rm w} = 10^{-8}\,M_\odot\,{\rm yr^{-1}}$, and $v_{\rm w} = 10\,{\rm km\,s^{-1}}$) due to the single crossing through the jet with the luminosity of $L_{\rm j} = 10^{42}\,{\rm erg\,s^{-1}}$ and the opening angle of 25°. Toward $z_{\rm stag}$, the mass removal due to a single encounter approaches the mean value of $\overline{\Delta M_{\rm l}} = \Delta M_{\rm l}^{\rm max}(z = z_{\rm stag}) = \Delta M_{\rm l}^{\rm min}(z = z_{\rm stag})$,

$$\frac{\overline{\Delta M_{\rm l}}}{M_\odot} = \frac{\dot m_{\rm w} v_{\rm w} R_\star^2}{4 G m_\star} = 2.9 \times 10^{-11}\left(\frac{\dot m_{\rm w}}{10^{-8}\,M_\odot\,{\rm yr^{-1}}}\right)\left(\frac{v_{\rm w}}{10\,{\rm km\,s^{-1}}}\right) \times \left(\frac{R_\star}{100\,R_\odot}\right)^2\left(\frac{m_\star}{1\,M_\odot}\right)^{-1}. \quad (17)$$

Because of the estimated several thousands of red giant–jet encounters according to Equation (13), the cumulative mass loss from the red giant can be derived as $\Delta M \sim n_{\rm cross}\Delta M_{\rm l}$, giving

$$\frac{\Delta M}{M_\odot} \approx 10^{-4}\left(\frac{L_{\rm j}}{10^{42}\,{\rm erg\,s^{-1}}}\right)\left(\frac{R_\star}{100\,R_\odot}\right)^4\left(\frac{z}{0.01\,{\rm pc}}\right)^{-\frac{7}{2}} \times \left(\frac{\theta}{0.22}\right)^{-2}\left(\frac{m_\star}{M_\odot}\right)^{-1}\left(\frac{t_{\rm jet}}{0.5\,{\rm Myr}}\right)\left(\frac{M_\bullet}{4 \times 10^6\,M_\odot}\right)^{\frac{1}{2}}. \quad (18)$$

In Figure 5, we plot ΔM for $L_{\rm j} = 10^{42}$ and $10^{44}\,{\rm erg\,s^{-1}}$, and $R_\star = 50$ and $100\,R_\odot$. Additionally, we plot ΔM for the longer jet lifetime of $t_{\rm jet} = 1\,{\rm Myr}$ and $L_{\rm j} = 10^{44}\,{\rm erg\,s^{-1}}$ and $R_\star = 100\,R_\odot$, which can be considered as an upper limit of ΔM for a red giant orbiting Sgr A*. We find that ΔM within the S cluster is comparable to the mass removal inferred from

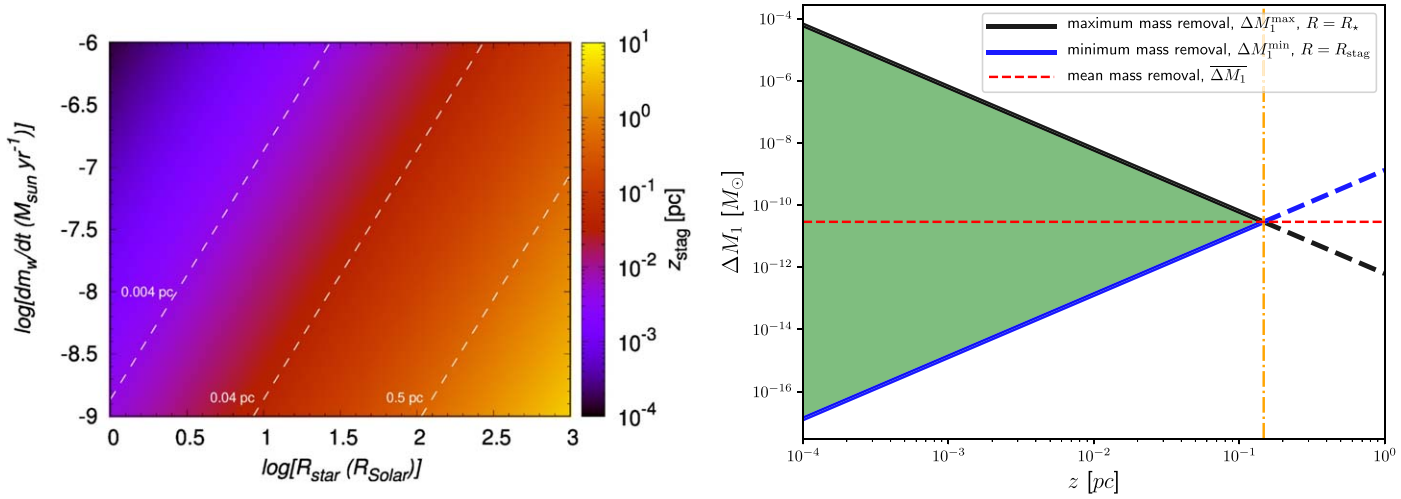

Figure 4. Mass removal during a single encounter of the red giant with the jet. Left panel: the color-coded distance in parsecs from Sgr A*, where $R_\star = R_{\rm stag}$ as a function of $\dot{m}_{\rm w}$ and $R_\star$. The dashed white lines mark $z_{\rm stag}$ equal to 0.004 pc, 0.04 pc, and 0.5 pc from the left to the right, respectively. Right panel: an exemplary mass removal range $\Delta M_{\rm l}^{\rm min}$–$\Delta M_{\rm l}^{\rm max}$ (green-shaded region) for $R_\star = 100\,R_\odot$, $\dot{m}_{\rm w} = 10^{-8}\,M_\odot\ {\rm yr}^{-1}$, $v_{\rm w} = 10\ {\rm km\ s}^{-1}$, $L_{\rm j} = 10^{42}\ {\rm erg\ s}^{-1}$, and $\theta = 12.^\circ5$. The dotted–dashed vertical orange line marks $z_{\rm stag}$ (see Equation (16)), where $R_\star = R_{\rm stag}$. The red dashed line marks the mean mass removal $\overline{\Delta M_{\rm l}}$ (see Equation (17)), $\overline{\Delta M_{\rm l}} = \Delta M_{\rm l}^{\rm max}(z = z_{\rm stag}) = \Delta M_{\rm l}^{\rm min}(z = z_{\rm stag})$.

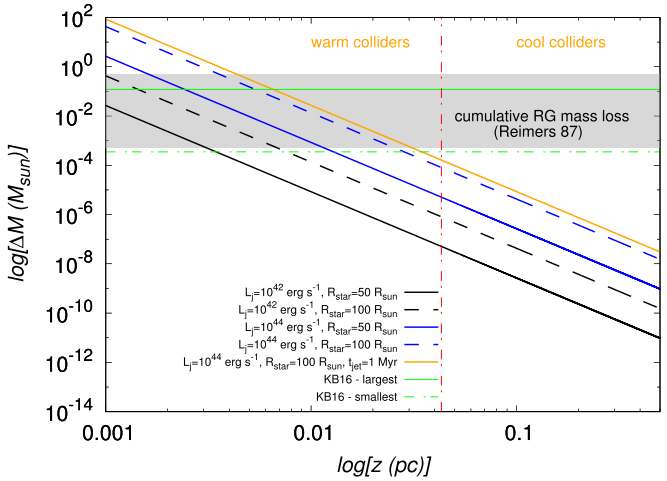

Figure 5. Cumulative mass removal ΔM due to the repetitive red giant–jet encounters as a function of the distance from Sgr A*. We fixed $L_{\rm j} = 10^{42}$ and $10^{44}\ {\rm erg\ s}^{-1}$ and $R_\star = 50$ and $100\,R_\odot$. In addition, we plot ΔM for $L_{\rm j} = 10^{44}\ {\rm erg\ s}^{-1}$, $R_\star = 100\,R_\odot$, and a longer duration of the jet activity, $t_{\rm jet} = 1$ Myr. For comparison, we also show the mass removal limits as inferred by Kieffer & Bogdanović (2016) for the red giant–clump collisions and the mass range as expected from the cumulative red giant (RG) mass loss due to stellar winds analyzed by Reimers (1987). The red dotted–dashed line marks the division between warm and cool colliders according to Equation (12).

the red giant–clump collision simulations by Kieffer & Bogdanović (2016). In Figure 5, we plot the upper and lower limits of ΔM obtained by Kieffer & Bogdanović (2016). Beyond $z = 0.03$ pc, ΔM for the star–jet interaction is progressively smaller than $3.5 \times 10^{-4}\,M_\odot$, which implies that the jet impact on the stellar evolution is the most profound for S-cluster red giants. In this region, there also lies the division between the warm and the cool colliders as discussed in Section 2.1, with warm colliders present inside $z_{\rm c} \sim 0.04$ pc, which is also marked in Figure 5 with a vertical dotted–dashed line. Because warm colliders are warmer and bigger, this further enhances the mass removal inside the S cluster. In addition, the mass removal due to the jet interaction is of a comparable order of magnitude to the mass loss expected from cool winds during the time interval of the active jet $\Delta M_{\rm w} \approx \dot{m}_{\rm w} t_{\rm jet} \sim 0.5$–$5 \times 10^{-4}\,M_\odot$ when $\dot{m}_{\rm w} \approx 10^{-6}$–$10^{-9}\,M_\odot\ {\rm yr}^{-1}$ (Reimers 1987), as indicated by the shaded rectangle in Figure 5. This implies that the jet–star interaction perturbs the stellar evolution of passing red giants, in particular in the innermost parts of the NSC.

Note that, on one hand, ΔM is supposed to be a lower limit as after the first passage through the jet, the giant is expected to expand to an even larger radius before the next encounter, which increases the mass removal efficiency (Kieffer & Bogdanović 2016). On the other hand, the resonant relaxation of stellar orbits as well as a jet precession may change the frequency of the jet–star interactions (see Sections 4 and 6.1), and therefore, $n_{\rm cross}$ should be considered as an upper limit of the number of encounters. Overall, ΔM in Equation (18) can be applied as an approximation for the total mass removal due to the red giant–jet interactions. Hence, the truncation of stellar envelopes of late-type stars by the jet during active phases of Sgr A* appears to be efficient and complementary to other previously proposed processes, mainly tidal disruptions of giants and stellar collisions with other stars and/or the accretion disk.

3. Missing Red Giants in the Near-infrared Domain

Red giants are post-main-sequence evolutionary stages of stars with initial mass $0.5\,M_\odot \lesssim m_\star \lesssim 10 M_\odot$. These stars exhausted hydrogen supplies in their cores, and the hydrogen fusion into helium continues in the shell. As a result, the mass of the helium core gradually increases, and this is linked to the increase in the atmosphere radius as well as luminosity. Stellar evolutionary models of red giants show that their atmosphere radius and bolometric luminosity depend primarily on the mass of the helium core $m_{\rm c}$ as (Refsdal & Weigert 1971;

Joss et al. 1987)

$$\frac{L_\star}{L_\odot} \approx \frac{10^{5.3}\mu_c^6}{1 + 10^{0.4}\mu_c^4 + 10^{0.5}\mu_c^5},$$
$$\frac{R_\star}{R_\odot} \approx \frac{3.7 \times 10^3 \mu_c^4}{1 + \mu_c^3 + 1.75\mu_c^4}, \quad (19)$$

where $\mu_c \equiv m_c/M_\odot$. This also holds for red supergiants with carbon–oxygen cores and burning hydrogen and helium in their shells (Paczyński 1970). In the red giant stage, the dominant energy source is the p–p process, and hence, the luminosity is mainly determined by the growth rate of the helium core $\dot{m}_c$,

$$\frac{L_\star}{L_\odot} \simeq 1.02\left(\frac{\dot{m}_c}{10^{-11}\,M_\odot\,\mathrm{yr}^{-1}}\right). \quad (20)$$

Equations (19) and (20) imply that the bolometric luminosity is not significantly affected by the jet–red giant interaction, as only the tenuous shell is ablated by the jet, and the dense core is left untouched. Then, the effective temperature T_1 of the ablated giant is

$$\frac{T_1}{T_0} = \left(\frac{R_0}{R_1}\right)^{\frac{1}{2}}, \quad (21)$$

where T_0 is the original effective temperature, and R_0 and R_1 are the atmosphere radii before and after the truncation, respectively. Here we implicitly assume that the red giant underwent $n_{\rm coll}$ interactions with the jet during the active phase given by Equation (13), which eventually leads to the decreased radius of $R_1 \approx R_{\rm stag}$ according to Equation (6). The luminosity in the infrared domain between frequencies ν_1 and ν_2 can be expressed using the Rayleigh–Jeans approximation[9] as $L_{\rm IR} \lesssim 8/3(\pi/c)^2 R_\star^2 k_B T_\star(\nu_2^3 - \nu_1^3) \propto R_\star^2 T_\star$ (see Alexander 2005 for a similar analysis), which using Equation (21) leads to

$$\frac{L_1}{L_0} \sim \left(\frac{R_1}{R_0}\right)^{\frac{3}{2}}. \quad (22)$$

For instance, the ablation of a red giant atmosphere from 120 to 30 $R_\odot$ would result in the increase of effective temperature by a factor of 2 and a decrease by a factor of 8 in the IR luminosity or ∼2.26 mag. The ablation of the envelope from 120 to $4R_\odot$ would result in the decrease by as much as ∼5.5 mag. The difference of 2–5 mag can already affect the count rate of late-type stars in the near-infrared domain in the central arcsecond of the Galactic center.

As an exemplary case, we set up a simplified temporal evolution of a red giant using Equations (19) and (20). We perform this calculation to estimate the potential difference in near-infrared magnitudes, and the color change for late-type stars before and after the active jet phase—it does not represent realistic stellar evolution tracks, but can provide insight into the basic trends in the near-infrared magnitude evolution and the effective temperature. We evolve the stellar luminosity and the radius for an increasing core mass $\mu_c = \mu_{c\,0} + \dot{\mu}_c dt$, where $\mu_{c\,0} = 0.104$ and the time step is $dt = 10^4$ yr. The overall evolution from $\mu_{c\,0}$ to $\mu_c = 0.55$ takes ∼8.41×10^9 yr, when neither the effect of stellar winds nor that of rotation is taken into account. The initial and the final core masses were chosen according to the limiting values for lighter stars, $m_\star < 2\,M_\odot$, in which case $\mu_c^{\rm min} \sim 0.1$ and $\mu_c^{\rm max} \sim 0.5$. These are stars with degenerate helium cores and hydrogen-burning shells (Refsdal & Weigert 1971). The lower core-mass value of 0.1 also approximately corresponds to the Schönberg–Chandrasekhar limit. The total duration is comparable to the time that stars of $1\,M_\odot$ spend on the giant and asymptotic giant branches, which is of the order of 10^9 yr according to MacLeod et al. (2012).

To assess the observational effects of the star–jet collision in the near-infrared domain, we calculate the effective temperature at each step using $T_\star = T_\odot(L_\star/L_\odot)^{1/4}(R_\star/R_\odot)^{-1/2}$. Subsequently, we calculate the monochromatic flux density in K band (2.2 μm) and L' band (3.8 μm) using $F_\nu = (R_\star/d_{\rm GC})^2\pi B_\nu(T_\star)$, where $B_\nu(T_\star)$ is the spectral brightness given by the Planck function at the given effective temperature. The corresponding magnitudes are calculated using $m_K = -2.5\log(F_K/653\ \mathrm{Jy})$ and $m_{L'} = -2.5\log(F_K/253\ \mathrm{Jy})$, from which the color index follows as $CI = m_K - m_{L'}$.

For the analysis in this section as well as in Section 5, we calculate intrinsic stellar magnitudes m_K and $m_{L'}$. The calculated magnitudes and colors can then be compared to extinction-corrected magnitudes and the derived surface-brightness profiles of the nuclear star cluster, i.e., those corrected for the foreground extinction. To compare our results to observed magnitudes and derived surface profiles that are just corrected for the differential extinction but not for the foreground extinction (Buchholz et al. 2009; Habibi et al. 2019; Schödel et al. 2020), it is necessary to increase the magnitudes using the corresponding mean extinction coefficients (see, e.g., Schödel et al. 2010), in particular $A_K = 2.54 \pm 0.12$ mag and $A_{L'} = 1.27 \pm 0.18$ mag.

The imprint of the ablation of the stellar atmosphere by a jet, whose kinetic luminosity is fixed to $L_j = 2.3 \times 10^{42}$ erg s^{-1}, is modeled by assuming that the radius of an interacting red giant keeps evolving according to Equation (19) when $R_\star < R_{\rm stag}$ at a given distance z from Sgr A*. After the stellar radius reaches the scale of the stagnation radius at a given distance z, we set $R_\star = R_{\rm stag}$ for the rest of the evolution, which can by justified by the fact that the red giant propagates through the jet $n_{\rm coll}$ times and the envelope is removed after repetitive encounters. The expected number of encounters is 6×10^5, 2×10^4, and 632 for $z = 0.001$ pc, 0.01 pc, and 0.1 pc, respectively; see Equation (13). In Figure 6, we show three magnitude–effective temperature curves of the ablated red giants that underwent repetitive encounters with the jet at their orbital distances of 0.001, 0.01, and 0.1 pc from Sgr A*, which led to their truncation to a smaller radius close to the corresponding stagnation radius at a given distance. In addition, we compare the magnitude–temperature curves of ablated giants with an unaffected evolution. We list the stellar parameters at the time of the atmosphere truncation when $R_\star = R_{\rm stag}$ at the corresponding distance as well as the parameters for the final state of ablated giants in Table 1. This is compared to an unaffected final state with the core mass of $0.55\,M_\odot$; see the bottom row of Table 1. The basic signature of the jet–star interaction is that the star gets progressively warmer (with a bluer, more negative color index) and fainter in the near-infrared K_s band in comparison with the normal evolution without any atmosphere ablation. This trend is more apparent for red giants that are

[9] Strictly speaking, for $T_\star = 5000$ K, the condition $k_B T_\star > h\nu$ applies for wavelengths longer than 2.9 μm.

Table 1
Parameters at the Time of the Jet Ablation and Those of the Final State of a Red Giant, which is Evolved from the Core Mass of $\mu_c = 0.104$ to 0.55

Ablation Distance (pc)	Ablation Time (yr)	$R_\star^{abl}$ ($R_\odot$)	$T_\star^{abl}$ (K)	$T_\star^{fin}$ (K)	m_K^{abl} (mag)	m_K^{fin} (mag)	CI^{fin}
0.001	3.0×10^8	0.45	6205	68 759	19.6	16.4	−0.14
0.01	8.0×10^9	4.45	4662	21 744	15.2	12.8	−0.09
0.1	8.4×10^9	44.51	3526	6 876	10.7	9.4	−0.09
Normal Evolution	⋯	255.21 (final radius)	⋯	2 871	⋯	7.47	0.51

Note. The upper three lines contain parameters of the ablated red giants orbiting at distances 0.001, 0.01, and 0.1 pc (first column). The second column lists the time, at which the ablation occurred with respect to the initial state of $\mu_c = 0.104$. The third column lists the truncation radius, when $R_\star = R_{stag}$. The fourth column lists the effective temperature at the time of truncation. The fifth column lists the final effective temperature at the final stage of their evolution (when $\mu_c = 0.55$). The sixth and seventh columns contain dereddened magnitudes at the ablation and final times, respectively. The last column contains dereddened color indices, $CI = m_K - m_L$, at the final state. The bottom line corresponds to the final state of a normal, unaffected evolution.

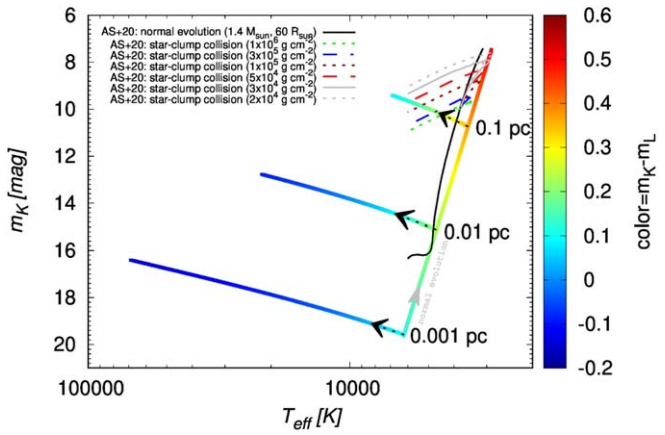

Figure 6. Near-infrared magnitude (K band, 2.2 μm, dereddened) and temperature (or color index that is color-coded) of a red giant after crossing the jet n_{coll} times. We compare three temperature–K_s-band magnitude curves affected by a series of collisions with the jet at $z = 0.001$, 0.01, and 0.1 pc (marked by black arrows) with a normal, unaffected evolution (marked by a gray arrow). The evolution is driven by an increase in the helium core mass from $\mu_c = 0.104$ to 0.55 $M_\odot$ with a time step of 10^4 yr. At each time step, we calculate $R_\star$ and $L_\star$ using Equations (19). The overall evolution takes $\sim 8 \times 10^9$ yr. For comparison, we also show the evolutionary tracks for the normal evolution (black solid line) and the evolution affected by the star–clump collisions (lines according to the legend for different clump surface densities listed in parentheses) as calculated by Amaro-Seoane et al. (2020, abbreviated as AS+20) using the CESAM code (Morel & Lebreton 2008).

closer to Sgr A* because of the smaller jet–star stagnation radius and hence a larger fraction of the stellar atmosphere that is removed.

Although we do not calculate stellar evolutionary tracks, only basic trends in terms of near-infrared magnitude and effective temperature, our results are consistent with those of Amaro-Seoane et al. (2020) who calculated evolutionary tracks specifically for late-type stars ablated due to the red giant–accretion-clump collisions. They show in their Figure 2 that the collision affects the stellar evolution of a red giant in a way that after repetitive encounters it follows a track along a nearly constant absolute bolometric magnitude toward higher effective temperatures. The constant absolute bolometric magnitude or bolometric luminosity in combination with an increasing effective temperature results in the drop in the near-infrared luminosity, because $L_{IR}/L_{bol} \propto T_\star^{-3}$. We used their evolutionary tracks calculated using the CESAM code (Morel & Lebreton 2008) for estimating K_s-band near-infrared magnitudes. These tracks are depicted in Figure 6 for the case of a normal evolution of a star with $M_\star = 1.4\,M_\odot$ and $R_\star = 60\,R_\odot$ (black solid line) and different collision cases for clumps with surface densities in the range $\Sigma = 2 \times 10^4$–10^6 g cm^{-2} (see the legend). Qualitatively, the perturbed stellar evolutionary tracks follow the temperature trends that we can also observe for giant–jet collisions: ablated giants move toward higher effective temperature. Also, they become fainter in the near-infrared domain in comparison with an unperturbed evolution. The main difference in comparison with the analysis of Amaro-Seoane et al. (2020) is their trend toward larger magnitudes (stars become fainter), while we see a small gradual increase in brightness. This difference is due to our simplifying assumption of a constant radius after the series of collisions with the jet, while in reality the radius should evolve, especially after the jet ceases to be active. Because $L_{IR} \propto R_\star^2 T_\star$, the near-infrared luminosity grows linearly with increasing temperature for the fixed stellar radius. This motivates further exploration of the effect of star–jet collisions using a modified stellar evolutionary code.

For asymptotic giant branch stars, an extreme transition from a red, cool luminous giant to a hot and faint white dwarf is possible when it is completely stripped of its envelope. This was studied by King (2020) for tidal stripping close to the SMBH but cannot be excluded also for asymptotic giant branch stars and jet collisions for a case when the giant star is at milliparsec separation from Sgr A* and less, in which case the stagnation radius is typically a fraction of the solar radius. In fact, an active jet can enlarge the volume around the SMBH where asymptotic giant branch stars are turned into white dwarfs. Considering Equation (6), we can derive that in order for R_{stag} to be of the order of a white-dwarf radius $R_{wd} \sim 0.01 R_\odot$, the giant needs to orbit the SMBH at $z \approx 0.15$ mpc so that the jet with $L_j = 10^{44}$ erg s^{-1} can truncate it down to the white-dwarf size. The stellar interior that is not affected by tidal forces is characterized by the Hill radius

$$r_{Hill} \approx z\left(\frac{m_\star}{3M_\bullet}\right)^{\frac{1}{3}} = 29\left(\frac{z}{0.15\ \mathrm{mpc}}\right) \times \left(\frac{m_\star}{1\,M_\odot}\right)^{\frac{1}{3}}\left(\frac{M_\bullet}{4 \times 10^6\,M_\odot}\right)^{-\frac{1}{3}} R_\odot, \quad (23)$$

from which we see that tidal forces alone will not truncate the giant down to its white-dwarf core because $r_{Hill} > R_{stag}$ at z.

In summary, the jet–star interaction could have affected the appearance of late-type giants in the central arcsecond by making them warmer or bluer in terms of color and hence fainter in the near-infrared domain.

4. Fraction of Red Giants Interacting with the Jet

We estimate the number of late-type stars, i.e., stars that form a cusp, that could have passed and interacted with the jet during its estimated lifetime of ∼0.1–0.5 Myr (Guo & Mathews 2012). For the density distribution of late-type stars in the inner 0.5 pc, we adopt a cusp-like power-law distribution $n_{\rm RG} \approx n_0 (z/z_0)^{-\gamma}$, with $n_0 \simeq 52\,{\rm pc}^{-3}$, $z_0 \simeq 4.9$ pc, and $\gamma \simeq 1.43$ (Gallego-Cano et al. 2018). The expected number of late-type stars within a certain distance $z_{\rm out}$ is

$$N_\star(<z_{\rm out}) = \int_0^{z_{\rm out}} n_{\rm RG}(z) 4\pi z'^2 dz' = 4\pi n_0 \frac{z_0^\gamma z_{\rm out}^{3-\gamma}}{3-\gamma} \quad (24)$$

giving $N_\star \approx 610$ and 25.8 inside 0.3 and 0.04 pc, respectively. The number of stars inside the jet at any time is given by the jet covering factor $f_{\rm j}$ in a spherical volume $V_\star = (4/3)\pi z_{\rm out}^3$. By considering a conical jet and a counter-jet with the total volume $V_{\rm j} = 2/3\pi R_{\rm j}^2 z_{\rm out}$, the covering factor is $f_{\rm j} = V_{\rm j}/V_\star \sim (R_{\rm j}/z_{\rm out})^2$ and the number of red giants inside the jet is $N_{\rm j}(<z_{\rm out}) = f_{\rm j} N_\star(<z_{\rm out}) \sim N_\star(<z_{\rm out})\tan^2(\theta)/2$. Then, the average number of red giants that are simultaneously inside the jet is $N_{\rm j} \approx 14.8$ and 0.62 inside 0.3 pc and 0.04 pc, respectively.

To estimate the number of stars crossing the jet per orbital timescale, we first calculate the jet-crossing rate per unit of time. Because we focus on the region $z \lesssim 0.5$ pc, which is well inside the radius of influence of Sgr A*, $r_{\rm h} \sim 2$ pc (Merritt 2013), we approximate the stellar velocity dispersion by the local Keplerian velocity, $\sigma_\star \sim v_{\rm orb} = \sqrt{GM_\bullet/z}$; see, e.g., Šubr & Haas (2014). With the jet cross section $S_{\rm jet} \approx z R_{\rm j} \sim z^2 \tan\theta$, the number of late-type stars entering both the jet and counter-jet per unit of time is

$$\dot{N}_{\rm RG} \approx 2 n_{\rm RG} \sigma_\star S_{\rm jet} \simeq 2 n_0 z_0^\gamma \sqrt{GM_\bullet} \tan\theta z^{\frac{3}{2}-\gamma}. \quad (25)$$

The number of red giants crossing the jet per orbital timescale is

$$N_{\rm RG} = \dot{N}_{\rm RG} P_{\rm orb} = 4\pi n_0 z_0^\gamma \tan\theta z^{3-\gamma}, \quad (26)$$

where the orbital period in the sphere of influence of the SMBH follows from the third Keplerian law, $P_{\rm orb} = 2\pi z^{3/2}/\sqrt{GM_\bullet}$. In Figure 7, we plot $N_{\rm RG}$. The average number of crossing giants per orbital period in the region with an outer radius $z_{\rm out}$ is

$$\overline{N}_{\rm RG} = \frac{4\pi}{4-\gamma} n_0 z_0^\gamma \tan\theta z_{\rm out}^{3-\gamma}. \quad (27)$$

In particular, $\overline{N}_{\rm RG} \simeq 3.5$ and $\overline{N}_{\rm RG} \simeq 82$ when $z_{\rm out} = 0.04$ pc (S cluster) and $z_{\rm out} = 0.3$ pc, respectively (see Figure 7).

In this case, $\overline{N}_{\rm RG}$ represents all late-type stars that cross the jet sheath per orbital period on average. The fraction of giants whose envelopes could have been stripped off by the jet can be estimated by comparing the radii of stars with the corresponding stagnation radius at a certain distance from Sgr A*. The basic condition for the ablation is that $R_\star \gtrsim R_{\rm stag}$ at a given z from Sgr A*. In particular, for $z = 0.04$ pc and the jet luminosity of $L_{\rm j} = 10^{42}\,{\rm erg\,s^{-1}}$, the minimum stellar parameters for ablation are $R_\star = 27\,R_\odot$, $\mu_{\rm c} = 0.3$, $L_\star = 129\,L_\odot$, $T_\star = 3743$ K, and $m_{\rm abl} = 11.7$ mag, where $m_{\rm abl}$ denotes the upper magnitude limit, below which stars are expected to be affected by the jet. Using the K-band luminosity function

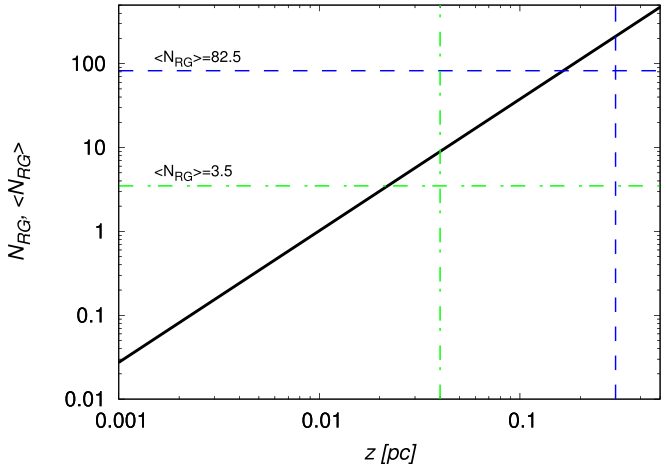

Figure 7. Number of red giants crossing the jet per orbital period (black solid line; see Equation (26)). The average number of red giant/jet interactions at $z \leqslant 0.04$ pc and 0.3 pc are plotted in green dotted–dashed and blue-dashed lines, respectively.

approximated by the power law, $d\log N/dm_{\rm K} = \beta$ with $\beta \simeq 0.3$ for late-type stars (Buchholz et al. 2009; Pfuhl et al. 2011) between 12 and 18 mag, we can estimate the fraction of ablated stars as $\eta = N_{\rm abl}/N_{\rm tot} \times 100 = 10^{\beta(m_{\rm abl}-m_{\rm max})+2}\%$, where $m_{\rm max}$ is the limiting magnitude, which we set to 18 mag according to Pfuhl et al. (2011). Then, for $z = 0.04$ pc and $L_{\rm j} = 10^{42}\,{\rm erg\,s^{-1}}$, we get $\eta = 1.27\%$. For the larger distance $z = 0.5$ pc and $L_{\rm j} = 10^{42}\,{\rm erg\,s^{-1}}$, we obtain the minimum parameters of ablated stars as follows, $R_\star = 338\,R_\odot$, $\mu_{\rm c} = 0.6$, $L_\star = 6081\,L_\odot$, $T_\star = 2775$ K, $m_{\rm abl} = 6.95$ mag with $\eta = 0.05\%$. The limiting values and the percentage of ablated giants are quite sensitive to the jet luminosity. Increasing $L_{\rm j}$ to $10^{44}\,{\rm erg\,s^{-1}}$, we get $R_\star = 2.7\,R_\odot$, $\mu_{\rm c} = 0.16$, $L_\star = 3.97\,L_\odot$, $T_\star = 4960$ K, $m_{\rm abl} = 16.1$ mag with $\eta = 26.5\%$ for $z = 0.04$ pc and $R_\star = 33.8\,R_\odot$, $\mu_{\rm c} = 0.31$, $L_\star = 181\,L_\odot$, $T_\star = 3645$ K, $m_{\rm abl} = 11.3$ mag with $\eta = 0.95\%$ for $z = 0.5$ pc. We summarize the relevant values in Table 2. Although the fraction of affected late-type stars is small, it significantly affects brighter stars with smaller magnitudes—stars brighter than 14 mag constitute ∼6.3% of the total observed sample and stars brighter than 12 mag constitute only 1.6%. We explicitly show the change in the projected brightness distribution for brighter stars in Section 5.

The jet ablation could partially have contributed to the inferred four to five missing late-type giants in the region with $z_{\rm out} = 0.04$ pc (Habibi et al. 2019) as well as to the ∼100 missing late-type giants in the larger region with $z_{\rm out} = 0.3$ pc (Gallego-Cano et al. 2018), especially for higher luminosities of the jet.

The number of stars that can interact with the jet is increased via dynamical processes in the dense nuclear star cluster. In particular, the vector resonant relaxation (VRR) changes the direction of the orbital angular momentum (Alexander 2005; Merritt 2013), and therefore, stars that were not passing through the jet can do so on the resonant relaxation timescale. More precisely, in the sphere of influence of the SMBH, stars move on Keplerian ellipses, and the gravitational interactions between stars are correlated. Given the finite number of stars, there is a nonzero torque on a test star. During the time interval

Table 2
Limiting Minimal Stellar Radii, Maximum Apparent K-band Magnitudes (dereddened), and the Fraction of Ablated Giants for Two Distances from Sgr A* (0.04 and 0.5 pc) and Two Luminosities of Its Jet (10^{42} erg s^{-1} and 10^{44} erg s^{-1})

Distance	$L_{\rm j} = 10^{42}$ erg s^{-1}	$L_{\rm j} = 10^{44}$ erg s^{-1}
0.04 pc	$R_\star = 27\,R_\odot$, $m_{\rm abl} = 11.7$, $\eta = 1.27\%$	$R_\star = 2.7\,R_\odot$, $m_{\rm abl} = 16.1$, $\eta = 26.5\%$
0.5 pc	$R_\star = 338\,R_\odot$, $m_{\rm abl} = 6.95$, $\eta = 0.05\%$	$R_\star = 33.8\,R_\odot$, $m_{\rm abl} = 11.3$, $\eta = 0.95\%$

Δt, for which $P_{\rm orb} \ll \Delta t \ll T_{\rm coh}$ and the coherence timescale

$$T_{\rm coh} = \frac{P_{\rm orb}}{2\pi\sqrt{N_\star}}\frac{M_\bullet}{m_\star} = \sqrt{\frac{3-\gamma}{4\pi G n_0 z_0^\gamma}}\frac{M_\bullet^{\frac{1}{2}}}{m_\star} z^{\frac{\gamma}{2}} \quad (28)$$

is inversely proportional to the square root of the number of enclosed stars, the angular momentum of a test star changes linearly with time.

The inclination of stellar orbits would change by $\sim\pi$ only when $T_{\rm coh}(z) \lesssim t_{\rm j} \sim 0.1$–$0.5$ Myr and hence essentially all late-type stars could interact with the jet during its lifetime. The estimated number of enclosed stars in the S cluster ($z_{\rm out} \sim 0.04$ pc) is $26 < N_\star < 10{,}000$, where the lower limit considers only late-type stars according to the analysis by Habibi et al. (2019) and the upper limit stands for all the stars including compact remnants. The upper limit is supposed to be closer to the actual number of stellar objects because the number of old neutron stars and stellar black holes in the central arcsecond could be of that order of magnitude (Morris 1993; Deegan & Nayakshin 2007; Zhu et al. 2018). The total number of massive objects naturally affects the coherence timescale by more than an order of magnitude. In Figure 8, we plot $T_{\rm coh}$. We see that when $N_\star \sim 1000$ and more, $T_{\rm coh}$ is comparable to the lifetime of the jet in the inner parts of the S cluster. In summary, the coherent resonant relaxation makes the number of affected giants bigger and the estimates per orbital timescale $\overline{N}_{\rm RG}$ can be considered as a lower limit. Another more hypothetical effect that can enlarge the number of affected giants is the jet precession (see Section 6.1).

The VRR can affect the number of encounters, $n_{\rm cross}$; see Equation (13). In case $T_{\rm coh} > t_{\rm jet}$, i.e., for a smaller number of enclosed objects ($N_\star \lesssim 100$), $n_{\rm cross}$ is still mainly determined by $t_{\rm jet}$; see Equation (13). However, then the mean number of interacting giants $\overline{N}_{\rm RG}$ is also not significantly enlarged. On the other hand, if $T_{\rm coh} \lesssim t_{\rm jet}$, then $n_{\rm cross}$ is reduced approximately by a factor of $2\theta/\pi$, which assumes that the angular momentum vector shifts linearly with time during $T_{\rm coh}$. In that sense, the interaction timescale with the jet is $t_{\rm int} \sim T_{\rm coh}(2\theta/\pi)$. Considering $T_{\rm coh} \sim t_{\rm jet}$, the number of crossings is

$$n_{\rm cross}^{\rm RR} \sim 2800\left(\frac{T_{\rm coh}}{0.5\ {\rm Myr}}\right)\left(\frac{M_\bullet}{4\times10^6\,M_\odot}\right)^{\frac{1}{2}}\left(\frac{z}{0.01\ {\rm pc}}\right)^{-\frac{3}{2}}, \quad (29)$$

which is smaller by an order of magnitude in comparison with $n_{\rm cross}$.

5. Effect of Jet Ablation on the Surface-brightness Profile of a Nuclear Star Cluster

To assess the observational signatures of the jet ablation of late-type stars, we generate a mock spherical cluster of stars. Their initial spatial distribution follows $n_{\rm RG} = n_0(z/z_0)^{-\gamma}$ with $n_0 = 52$ pc^{-3}, $z_0 = 4.9$ pc, and $\gamma \sim 1.43$ (Gallego-Cano et al. 2018). This spatial profile suggests that there are in total ~4000 late-type stars inside the inner 1 pc, which we generate using the Monte Carlo approach to form a mock NSC; see Figure 9 (left panel) for illustration.

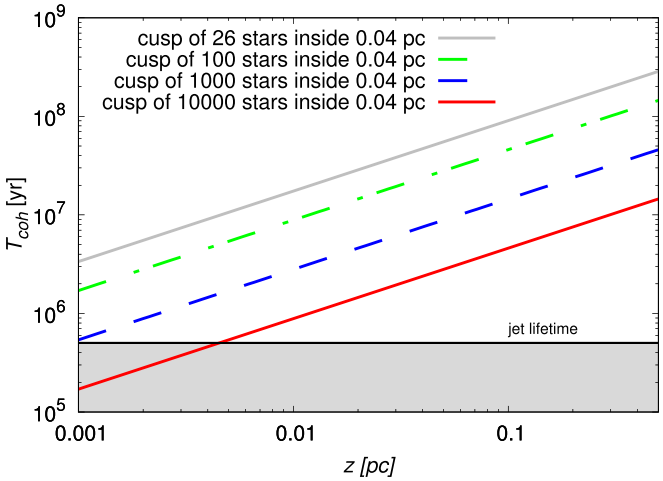

Figure 8. The coherence timescale $T_{\rm coh}$ for different numbers of stars in the S cluster according to the legend. The shaded area stands for the expected lifetime of the jet during the previous Seyfert-like activity of Sgr A*.

Each star is assigned its mass in the range from $0.08\,M_\odot$ to $100\,M_\odot$ following the initial mass function (IMF) according to Kroupa (2001), i.e.,

$$\zeta(m_\star) = m_\star^{-\alpha}, \ \text{where} \begin{cases} \alpha = 0.03, & m_\star < 0.08\,M_\odot, \\ \alpha = 1.3, & 0.08\,M_\odot < m_\star < 0.5\,M_\odot, \\ \alpha = 2.3, & m_\star > 0.5\,M_\odot. \end{cases} \quad (30)$$

The Chabrier/Kroupa IMF is a good approximation for the observed mass distribution of the late-type NSC population (Pfuhl et al. 2011).

In the next step, we assigned the core mass to each star of the mock cluster. Here, we fix the ratio between the core mass and the stellar mass to $\mu_{\rm c}/m_\star = 0.4$, which is in between the value inferred from the Schönberg–Chandrasekhar limit[10] and the final phases of the stellar evolution, where the white-dwarf core constitutes most of the mass for solar-type stars. For more precise simulations, core masses from the stellar evolution of the NSC should be adopted; however, here we are interested in the first-order effects of the jet activity on the surface-brightness distributions.

To construct the surface-brightness profiles of the late-type population after the active jet phase in different magnitude bins, we followed these steps:

[10] The Schönberg–Chandrasekhar limit expresses the ratio between the isothermal core mass and the stellar mass, $m_{\rm ic}/m_\star \simeq 0.37(\mu_{\rm env}/\mu_{\rm ic})^2 \sim 0.1$, where $\mu_{\rm env}$ and $\mu_{\rm ic}$ are the mean molecular weights for the envelope and the isothermal core, respectively.

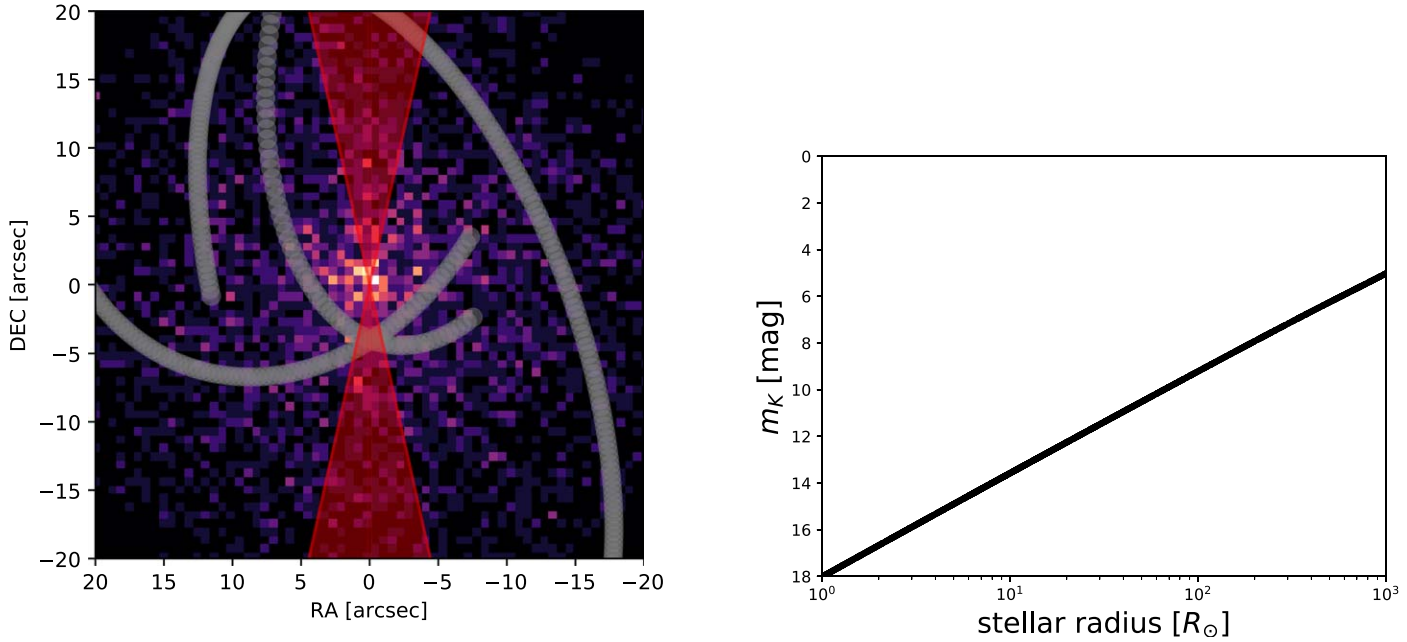

Figure 9. Initial properties of the Monte-Carlo-generated mock NSC. Left panel: the projected surface density distribution of 4000 stars with the illustrated active jet with the half-opening angle of $\theta = 12.^\circ5$. The gray streamers illustrate the mini-spiral arms according to the Keplerian model of Zhao et al. (2009). Right panel: the K-band magnitude (dereddened)–stellar radius relation for our generated NSC.

1. We calculated $L_\star(\mu_c)$ and $R_\star(\mu_c)$ using Equation (19).
2. If the jet was set active with a certain luminosity L_j, we compared $R_\star$ and R_{stag} for a given distance z of the star. If $R_\star \geqslant R_{stag}$, then we set $R_\star = R_{stag}$. In this case, we also implicitly assumed that at a given distance, all of the stars, for which $R_\star \geqslant R_{stag}$, are eventually ablated by the jet; hence, the resonant relaxation was assumed to be efficient and hence $T_{coh} < t_{jet}$.
3. We estimated the effective temperature of a star using $T_\star = T_\odot (L_\star/L_\odot)^{1/4}(R_\star/R_\odot)^{-1/2}$.
4. From the Planck function $B_\nu(T_\star)$, we calculated the monochromatic flux in the K_s band (2.2 μm) $F_\nu(R_\star, T_\star) = (R_\star/d_{GC})^2 \pi B_\nu(T_\star)$ and the corresponding apparent magnitude m_K (dereddened).

The initial relation between the K_s-band magnitude and the stellar radius is shown in Figure 9 in the right panel. We calculate the projected stellar density using concentric annuli with mean radius R and width of ΔR, $\sigma_\star = N_\star/(2\pi R \Delta R)$, where $N_\star$ is the number of stars in an annulus. We estimate the uncertainty of the stellar number counts as $\sigma_N \approx \sqrt{N_\star}$. Subsequently, we construct the surface stellar profiles in two-magnitude bins starting at $m_K = 18$ mag up to $m_K = 10$ mag, i.e., in total, four bins; see Figure 10. In the top-left panel of Figure 10, we plot the nominal projected distribution without considering the effect of the jet. The brightness profile for all four magnitude bins can be approximated by simple power-law functions, $N(R) = N_0(R/R_0)^{-\Gamma}$, whose slopes are listed in Table 3. Hence, the initial cluster distribution is cusp like. In the top-right panel, we show the case with an active jet with the luminosity of $L_j = 10^{42}$ erg s^{-1}. We see that the profile for the brightest stars in the 10–12 mag bin becomes flat in the inner arcsecond and can be described as a broken power-law function, $N(R) = N_0(R/R_{br})^{-\Gamma}[1 + (R/R_{br})^{\Delta}]^{(\Gamma-\Gamma_0)/\Delta}$, where R_{br} is a break radius, Γ is a slope of the inner part, Γ_0 marks the slope of an outer part, and Δ denotes the sharpness of the transition. The larger surface-brightness values for this magnitude bin may be interpreted as an extra input of ablated giants with initial magnitudes $m_K < 10$ mag that after the ablation fall into bins with a larger magnitude. Finally, we increase the jet luminosity to $L_j = 10^{44}$ erg s^{-1}, which makes the flattening of the brightest giants even more profound. The stars in the 12–14 mag bin also exhibit a flatter profile inside the inner arcsecond for this case, which shows the significance of the jet luminosity in affecting the observed surface profile of the NSC. We list the power-law slopes for both a simple and a broken power-law function and the break radii, where available, for all the magnitude bins and the three jet-activity cases in Table 3.

Figure 10 demonstrates a potential signature of the jet activity on the surface profile of the NSC. It is important to study differential profiles, i.e., the distribution in different magnitude bins, because the lower-luminosity jet starts affecting the profile of bright stars (smaller magnitudes), while with an increasing jet luminosity, the fainter stars become affected as well, starting at smaller projected radii ($<1''$). Our Monte Carlo simulation suggests that the active jet phase with $L_j \lesssim 10^{44}$ erg s^{-1} likely affected late-type stars with $m_K \leqslant 14$ mag that exhibit the flat profile inside the inner arcsecond. The fainter stars of $m_K > 14$ mag can still keep a cusp-like profile after the jet ceased its enhanced activity.

For better quantitative comparisons with observations, it is necessary to include the stars of different ages and hence different core masses. This is rather complex as there were recurrent star formation episodes in the NSC, with 80% of the stellar mass being formed 5 Gyr ago, the minimum in the star formation rate close to 1 Gyr, and the renewed star formation in the last 100–200 million years, although with the 10× lower star formation rate than at earlier episodes (Pfuhl et al. 2011). These findings were confirmed by Schödel et al. (2020), who estimate that 80% of stars formed 10 Gyr ago or earlier, then about 15% formed 3 Gyr ago, and the remaining fraction in the last 100 Myr. Furthermore, the dynamical effects such as the mass segregation and the relaxation processes could also have played a role in shaping the final observed profile of the NSC, and in addition, we might expect other bright-giant depletion

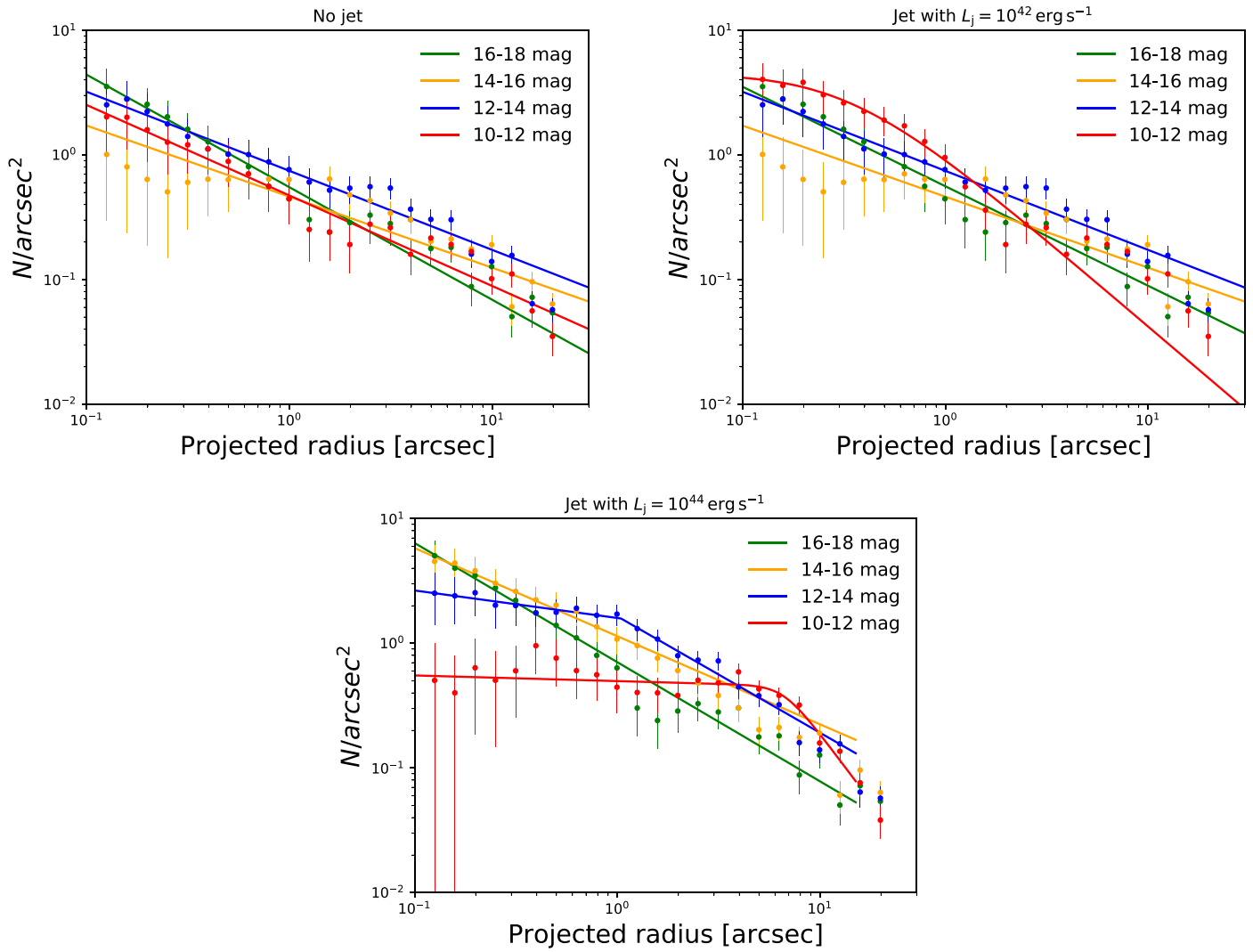

Figure 10. Potential effect of the jet activity on the surface distribution of the initially cuspy late-type NSC. The calculations assume that the coherent resonant relaxation timescale is comparable to or shorter than the jet lifetime (∼0.5 Myr) within the S-cluster region. In all panels, the magnitude bins are dereddened. Top-left panel: the projected profile of an initial cusp of late-type stars with the surface slope of $\Gamma \sim 0.6$–0.9 across all magnitude bins (2 mag bins). Top-right panel: a modified projected profile for the jet luminosity of 10^{42} erg s^{-1}. The 10–12 mag surface profile flattens inside the inner arcsecond, while the fainter stars (12–18 mag) keep a cusp-like profile. Bottom panel: a modified surface profile for the jet luminosity of $L_j = 10^{44}$ erg s^{-1}. The profile of the brightest stars (10–12 mag) flattens even more and decreases inside the inner arcsecond. The stars with 12–14 mag exhibit a flat profile as well in the inner arcsecond. The stars in the 14–16 mag and 16–18 mag bins keep the cuspy profile. For all three panels, the solid lines represent the single and the broken power-law function fits to the surface stellar distribution in four magnitude bins. The slopes and the break radii are listed in Table 3.

Table 3

Summary of the Power-law Slopes (for Both Single and Broken if Relevant) for the Four Magnitude Bins (2 mag Intervals Starting at 18 mag up 10 mag in the Near-infrared K_s Band; Magnitudes are Dereddened) and Three Jet-activity Cases (No Jet, $L_j = 10^{42}$ erg s^{-1}, $L_j = 10^{44}$ erg s^{-1})

Magnitude Bin	No Jet	Jet $L_j = 10^{42}$ erg s^{-1}	Jet $L_j = 10^{44}$ erg s^{-1}
18–16 mag	single: $\Gamma = 0.9$	single: $\Gamma = 0.8$	single: $\Gamma = 1.0$
16–14 mag	single: $\Gamma = 0.6$	single: $\Gamma = 0.6$	single: $\Gamma = 0.7$
14–12 mag	single: $\Gamma = 0.6$	single: $\Gamma = 0.6$	broken: $\Gamma = 0.2$, $\Gamma_0 = 0.9$, $R_{br} = 1''$
12–10 mag	single: $\Gamma = 0.7$	broken: $\Gamma = -0.08$, $\Gamma_0 = 1.4$, $R_{br} = 0''.3$	broken: $\Gamma = 0.04$, $\Gamma_0 = 2.2$, $R_{br} = 6''.6$

processes (Alexander 2005). Despite these difficulties in comparing theoretical and observed profiles, the basic trend shown in Figure 10, in particular for $L_j = 10^{44}$ erg s^{-1} (bottom panel), is consistent with the observational findings of Schödel et al. (2020), who found cusp-like profiles for all magnitude bins apart from the $m_K = 14.5$–14 mag bin (including foreground field extinction), which shows a flat/decreasing profile in their analysis. In our panels in Figure 10, this corresponds to the dereddened 10–12 and 12–14 mag bins, whose profiles become affected for $L_j = 10^{42}$ erg s^{-1} starting from the projected radii below $1''$. However, Schödel et al. (2020) also note that precise surface profiles for late-type stars are difficult to construct due to the contamination at all magnitude bins by an unrelaxed population of young stars.

Habibi et al. (2019) report a cusp-like profile for late-type stars of $m_K < 17$ mag (including foreground extinction), which approximately corresponds to our bin of 14–16 mag (yellow points) that maintains a cusp-like profile even for the largest jet luminosity (bottom panel). In conclusion, the expected trend of preferential depletion of bright late-type stars by the jet is confirmed.

6. Discussion

We investigated the effects of a jet during an active phase of Sgr A* in the last million years on the appearance of late-type giant stars with atmosphere radii more than $30R_\odot$. We found that especially in the innermost arcsecond of the Galactic center (the S cluster), the upper layers of the stellar envelope could be removed by the jet ram pressure. Hence, the jet–red giant interactions during the active phase of Sgr A* could have contributed to the depletion of bright late-type stars. In other words, the atmosphere ablation by the jet would alter the red giant appearance in a way that would make them look bluer and fainter in the near-infrared bands (mainly K' and L bands), in which stars in the Galactic center region are generally monitored. In the following, we outline several additional effects that could be associated with the jet/red giant interaction.

6.1. Enlarging the Number of Affected Stars by the Jet Precession

Jet precession is a phenomenon that accompanies the launching of jets during the evolution of galaxies and stellar binaries. It is caused by perturbations due to the misalignment of the accretion flow and the black hole spin, the so-called Lense–Thirring precession, or by a secondary black hole. The jet precession was proposed to explain a long-term flux variability in radio galaxies, e.g., OJ 287 (Britzen et al. 2018), 3C 84 (Britzen et al. 2019b), 3C 279 (Abraham & Carrara 1998), the neutrino emission from TXS 0506+056 (Britzen et al. 2019a), as well as in X-ray binaries (Monceau-Baroux et al. 2015; Miller-Jones et al. 2019).

For the Galactic center, the Lense–Thirring precession of the hot thick accretion flow was analyzed by Dexter & Fragile (2013) in relation to the near-infrared and millimeter variability of Sgr A*. This effect would also translate to the precession of the jet under the assumption that it is coupled to the disk via the launching mechanism (Blandford–Payne mechanism; see Blandford & Payne 1982). The jet precession is also suggested by wide UV ionization cones with the opening angle of 60∘ (Bland-Hawthorn et al. 2019), which is larger by a factor of a few expected for the jet opening angle of $\sim 25^\circ$ (Li et al. 2013).

We estimate the factor by which the volume of the affected red giants is enlarged. We adopt the jet precession half-opening angle of $\Omega_p \approx 30^\circ$ based on the scale of UV ionization cones (Bland-Hawthorn et al. 2019). During the precession motion, the jet circumscribes a cone with the radius $R_p = z \sin \Omega_p$. The factor by which the volume at given distance z enlarges is given by

$$f_{\rm prec} = \frac{2\pi R_p}{2R_j} = \pi \frac{\sin \Omega_p}{\tan \theta} \sim 7.1, \quad (31)$$

when $\theta = 12.^\circ 5$ and $\Omega_p = 30^\circ$. The number of affected late-type stars would then increase by the same factor to $N_j \approx 105$ and 4.4 within 0.3 and 0.04 pc, respectively, which is comparable to the number of missing bright red giants at these scales—100 at $z < 0.3$ pc (Gallego-Cano et al. 2018) and 4 at $z < 0.04$ pc (Habibi et al. 2019). The factor derived in Equation (31) should be treated as an upper limit on the volume enlargement as it assumes that the precession period is comparable to or less than the jet lifetime, but it could also be longer. On the other hand, a larger volume means that the stars are affected correspondingly less (over a shorter period of time) by the jet action, which is spread in different directions with the precession duty cycle.

6.2. High-energy Particle Acceleration and Jet Mass Loading due to Jet/Star Interactions

The detection of the Fermi bubbles in the GeV domain indicates the presence of relativistic particles emitting gamma rays. Guo & Mathews (2012) considered that particles can be accelerated in the jet-launching region or in the jet termination shocks. Note, however, that the coexistence of the jet with the dense NSC in the Galactic center makes jet/star interactions very likely. The NSC is composed of both early- and late-type stars. In the former case, the powerful wind of OB and Wolf–Rayet stars makes the stagnation distance $R_{\rm stag} \gg R_\star$, and therefore, a double bow-shock structure is formed (Araudo et al. 2013). In the latter case, the slow winds of low-mass stars cannot create a big bow shock around the stars, but a shock in the jet will be formed anyway. In both cases, particles can be accelerated through the Fermi I acceleration mechanism in the bow shocks (Bell 1978). Even when the interaction with massive stars is a better scenario to accelerate particles up to highest energies (given that the size of the acceleration region is $\sim R_{\rm stag}$), acceleration of particles up to GeV energies is not difficult to achieve.

Barkov et al. (2010, 2012b) consider the interaction of AGN jets with red giant stars to explain the TeV emission in radio galaxies and blazars. The mass stripped from the red giant forms clouds moving in the jet direction; see also our Figure 1. Particles are accelerated in the bow shock around the cloud formed by the pressure exerted by the jet from below. Another shock propagates into the cloud, and as a consequence, it will heat up and expand. After a certain time, there will be a population of relativistic particles in the jet as well as chemical enrichment by stellar envelopes (Perucho et al. 2017). These effects were previously not taken into account in the jet models of the Fermi bubbles.

6.3. Chemically Peculiar Stars as Remnant Cores of Ablated Red Giants

The past ablation of red giants by the jet would contribute to the apparent lack of late-type stars in the central region of the Galactic center. Another potential imprint of the past jet–red giant interaction would be the presence of chemically peculiar, high-metallicity stars in the NSC. This can be predicted from the fact that as the jet ram pressure removes upper hydrogen- and helium-rich parts of the stellar atmosphere, the lower metal-rich parts as well as the denser core are exposed. In fact, two late-type stars at ~ 0.5 pc from Sgr A* were reported as having a supersolar metallicity (Do et al. 2018) with an anomalous abundance of scandium, vanadium, and yttrium. A detailed modeling of the stellar evolution in combination with the treatment of the jet–star interaction is needed to confirm or exclude the previous interaction with the jet for these and similar candidate stars with supersolar metallicities.

6.4. A Collimated Jet or a Broad-angle Disk Wind?

In the current analysis, we took into account mainly highly collimated nuclear outflow—jet—with the small half-opening angle close to $\sim 10^{\circ}$. The analysis of the UV ionization cones by Bland-Hawthorn et al. (2019) indicates a half-opening angle of $\sim 30^{\circ}$, which could be a signature of jet precession as we discussed in Section 6.1 or alternatively disk winds with a larger opening angle. In case the jet would be absent and the disk wind would be present with the larger half-opening angle, the expected stagnation radius would be proportionally larger because $R_{\rm stag} \propto \tan\theta$. Assuming the same kinetic luminosity $L_{\rm j} = 10^{42}\,{\rm erg\,s^{-1}}$ and the outflow velocity close to c (ultrafast outflows), the ratio of the stagnation radii is $R_{\rm stag}^{\rm wind}/R_{\rm stag}^{\rm jet} = \tan\theta_{\rm wind}/\tan\theta_{\rm jet} \approx 2.6$, which yields for $R_{\rm stag}^{\rm wind} \sim 70\,R_{\odot}$ using Equation (6). The ablation effect would still take place but only for the largest red giants with $R_{\star} \gtrsim 100\,R_{\odot}$ at the outer radius of the S cluster. The stagnation radius of $30\,R_{\odot}$ would be reached at the distance of $z \sim 0.017\,{\rm pc}$ for the same stellar parameters as we assumed in Equation (6) and a larger outflow half-opening angle of 30o.

6.5. Recurrent Seyfert-like Activity and TDEs

The X-ray/γ-ray Fermi bubbles were created during the increased Seyfert-like activity about 3.5 ± 1 Myr ago (Bland-Hawthorn et al. 2019) with total duration of $\sim$0.1–0.5 Myr (Guo & Mathews 2012). Currently, it is unclear whether this increased activity is related to the star formation event that led to the formation of massive OB/Wolf–Rayet stars a few million years ago, a fraction of which forms a stellar disk that is a remnant of a former massive gaseous disk (Levin & Beloborodov 2003). In case a correlation between the episodic star formation and the accretion activity exists, the Seyfert-like phase could occur every 100 million years based on the currently observed stellar populations in the Galactic center region (Pfuhl et al. 2011). In the context of this work, this could provide a mechanism for the recurrent depletion of large red giants by the increased jet activity. However, the most relevant episode in terms of currently observed stellar populations is the most recent episode a few million years ago. There is evidence for even more recent activity $\sim$400 yr ago, which is inferred from the X-ray reflections or propagating brightening of molecular clouds in the Central Molecular Zone (Sunyaev et al. 1993; Sunyaev & Churazov 1998). However, these repetitive events occur stochastically based on the presence of infalling clumps and lead to the increase by only several orders of magnitude and last for several years depending on the exact viscous timescale (Czerny et al. 2013).

Another possibility of a recurrent launching of the jet is a TDE, which can occur in the Galactic center every $\sim 10^4$–10^5 yr depending on the stellar type (Syer & Ulmer 1999; Alexander 2005; Komossa 2015). For completeness, we note that the jet is not always formed during the TDE (Komossa 2015). However, for a few months to years, the TDE can trigger a jet activity similar to the Seyfert sources (Hills 1975). Due to the short duration of the TDE between several months to years given by the steep dependency of the luminosity on time, $L \propto t^{-5/3}$, the average number of interacting stars would be given by the estimates calculated in Section 4. In general, the number of ablated red giants in the S cluster would be of the order of unity. The jet precession driven by the Lense–Thirring effect (Lodato & Pringle 2006) could enlarge this number depending on the precession period and $\Omega_{\rm p}$ (see Section 6.1).

6.6. Comparison with Other Mechanisms—the Region of Efficiency

The jet-induced alternation of the population of late-type stars is not necessarily an alternative to other proposed mechanism, listed in the introductory, Section 1. In reality, it could have coexisted simultaneously during the past few million years with other previously proposed mechanisms, in particular the tidal disruption of red giant envelopes as well as direct star–disk interactions. This follows from the fact that these mechanisms have different length scales of their efficiency, as we further outline in the paragraphs below.

First, the tidal disruption of red giant envelopes takes place on the smallest scales—less than 1 mpc from Sgr A*—as given by the tidal radius, $r_{\rm t} \approx R_{\star}(2M_{\bullet}/m_{\star})^{1/3}$,

$$r_{\rm t} \lesssim 6000\left(\frac{R_{\star}}{30\,R_{\odot}}\right)\left(\frac{m_{\star}}{1\,M_{\odot}}\right)^{-\frac{1}{3}}\left(\frac{M_{\bullet}}{4\times 10^{6}\,M_{\odot}}\right)^{\frac{1}{3}} R_{\odot} = 0.14\ {\rm mpc} = 354 R_{\rm Schw}. \quad (32)$$

The resonant relaxation process (discussed in Section 4), in particular the scalar resonant relaxation, can cause an increase in orbital eccentricities and thus effectively induce the tidal disruption of giants as their orbital distance decreases below $r_{\rm t}$ close to the pericenter of their orbits. This could have contributed to the dearth of brighter red giants in the inner $\sim$0.1 pc (Madigan et al. 2011), which is a larger scale than given by $r_{\rm t}$ but still smaller than the total extent of 0.5 pc of the red giant hole.

Then, the jet-induced mass removal is clearly the most efficient in the S-cluster region, $z \lesssim 0.04$ pc, according to the cumulative mass removal distance profile in Figure 5. Another way to constrain the region of the maximum efficiency is to use the relation in Equation (6) for the stagnation radius, from which we derive the distance z. It follows that for the maximum jet luminosity of $L_{\rm j} = 10^{44}\,{\rm erg\,s^{-1}}$ and the stagnation radius range of $R_{\rm stag} = 4$–$30\,R_{\odot}$, we obtain the distance range $z_{\rm jet} = 0.06$–0.44 pc. Hence, within the S cluster, $z \lesssim 0.04$ pc, $R_{\rm stag}$ would be effectively below $4\,R_{\odot}$, which corresponds to $K \sim 16$ mag stars for a typical age of 5 Gyr. Therefore, the jet luminosities close to the Eddington limit for Sgr A* are required to truncate the atmospheres of late-type stars of $K \lesssim 16$ mag. For the moderate jet luminosity of $L_{\rm j} = 10^{42}\,{\rm erg\,s^{-1}}$, the distance range decreases by an order of magnitude to $z_{\rm j} = 0.006$–0.04 pc; hence, only brighter giants with $R_{\star} = 30\,R_{\odot}$ ($K \sim 13.5$ mag) would be effectively truncated within the S cluster, while the smaller and fainter giants with $K \sim 16$ mag would remain largely unaffected by the jet.

Finally, the star–clumpy disk collisions are the most efficient for the disk surface densities $\Sigma > 10^4\,{\rm g\,cm^{-2}}$ typical of self-gravitating clumps (Kieffer & Bogdanović 2016; Amaro-Seoane et al. 2020), which can form at larger distance scales where the condition for gravitational instability is met as given by the Toomre instability criterion (Milosavljević & Loeb 2004). In the Galactic center, this region likely corresponds to $0.04 \lesssim z \lesssim 0.5$ pc, where the disk population of young massive stars is observed, and they are believed to have formed in situ in a massive gaseous disk (Levin & Beloborodov 2003).

Hence, we speculate that the dearth of bright red giants for $z \lesssim 0.5$ pc is due to the combination of the three processes—tidal stripping, jet-induced atmosphere ablation, and star–disk interactions—that operated the most efficiently at complementary length scales up to ∼0.5 pc.

6.7. Observational Signatures and Falsifiability

The jet-ablation mechanism likely operated in the central S-cluster region (<0.04 pc) for stars of large atmosphere radii of $10\,R_\odot$, and especially for supergiants of $\sim 100\,R_\odot$ even at larger distances up to ∼0.1 pc. However, as the enhanced jet activity and the resulting atmosphere ablation took place a few million years ago, any direct observational trace of the jet–star interaction is difficult to find. Here we list tentative observational signatures of the jet ablation on the preexisting cusp of late-type stars. Some of them have more possible interpretations due to other mechanisms operating simultaneously in the complex NSC around Sgr A*. The signatures proposed here can serve as a guideline toward confirming the jet activity and in particular the jet–star interaction in the central parsec. On the other hand, if other explanations become more likely, these can also serve as suitable falsifiability criteria for the jet-ablation theory. The signatures can be outlined as follows:

(i) Flattening of the density distribution for brighter late-type stars. This is a classical signature of the preferential bright late-type star depletion, which has more interpretations due to mechanisms, which likely operated on different scales; see Section 6.6. Therefore, this signature should be treated with caution. However, we have shown in Section 5 that the jet active for a sufficiently long time can have an impact on the surface-brightness profile of the NSC when it reaches the kinetic luminosity at least 10^{42} erg s^{-1}; see also Section 5 and Figure 10. In particular, brighter giants with $m_K < 14$ mag could exhibit a flat profile due to the jet activity inside the inner arcsecond ($z \lesssim 0.04$ pc). Such a trend has also been recently reported by the high-sensitivity photometric analysis of Schödel et al. (2020).

(ii) Detection of high-metallicity stars. The jet ablation of red giant and supergiant shells could reveal deeper metal-rich layers. A jet-ablation mechanism can be considered as one of the explanations for the occurrence of stars with anomalous metal concentrations in their atmospheres, as was found by Do et al. (2018); see also Section 6.3.

(iii) Cluster of remnant white dwarfs at millipasec scales. In relation to point (ii), an extreme case of jet ablation could lead to the exposure of degenerate cores for asymptotic giant branch (AGB) stars. This is analogous to the ablation by tidal stripping (King 2020); however, the jet ablation has a larger length scale for Sgr A*. As we derived in Section 3, the AGB stars could be jet-ablated down to the white-dwarf cores for $z < 0.015$–0.15 mpc for $L_{\rm j} = 10^{42}$–10^{44} erg s^{-1}. The tidal stripping to the size of $10^{-2}\,R_\odot$ is only possible essentially below the event horizon. There has not been a direct observation of white dwarfs at such small distances from Sgr A*; however, the hard X-ray flux peaking at Sgr A* was hypothesized to originate in the cluster of accreting white dwarfs (Perez et al. 2015).

(iv) Cusp of remnant blue OB stars. As we have shown in Section 3, the late-type stars could be turned to blue stars of spectral type OB by the jet-ablation mechanism. In Table 1, we show that the effective temperature could be of a few $\times 10^4$ K, and with the stagnation radius of $R_{\rm stag} = 4.45\,R_\odot$, the K-band magnitude was estimated to reach $m_K \sim 13$ mag, which is comparable to an S2 star ($m_K \sim 14.1$ mag, Habibi et al. 2017). In this sense, we hypothesize that the fraction of S stars could be produced via the jet ablation of older stars; however, the production rate within the S cluster was of the order of unity, as we showed in Section 4. Hence, the majority of B-type S stars was most likely formed in situ in the circumnuclear gaseous material (Mapelli & Gualandris 2016), and the current location and the kinematic structure of the S cluster are a result of different dynamical processes, most likely the Kozai–Lidov mechanism and the resonant relaxation (Ali et al. 2020).

(v) Presence of bow-shock and comet-shaped sources. The presence of bow-shock sources X3 and X7 (Mužić et al. 2010) as well as X8 (Peißker et al. 2019) in the mini cavity implies the interaction of these sources with a nuclear outflow in the current state of activity of Sgr A*. The present nuclear outflow could be a signature of a low-surface-brightness jet (Yusef-Zadeh et al. 2020), which was much more luminous a few million years ago. The infrared-excess sources X3, X7, and X8 thus directly reveal the interaction of a nuclear outflow/jet with stars at the scale of ∼0.2 pc.

(vi) Nonspherical distribution of stars. In the broader context, the activity of the Seyfert-like jet at the scales of ∼0.1 pc could be imprinted on the nonspherical stellar structures, e.g., by affecting the distribution of denser star-forming material and its temperature via the jet feedback. Recently, Ali et al. (2020) revealed an X-shape structure of the S cluster formed by two, nearly perpendicular stellar disks. Because S stars formed a few million years ago, their formation could be linked to the phase of higher accretion and enhanced jet activity. Also, the X-structure implies that the resonant relaxation process (see Section 4), in particular the VRR, is not as fast; otherwise, the kinematic structure of the S cluster would be rather isotropic. However, the potential relation between the jet activity and the stellar kinematics needs to be verified via the detailed hydrodynamical/N-body or smooth-particle-hydrodynamics simulations.

(vii) Nonspherical distribution of ionization tracers around Sgr A*. In a similar way as we discussed in point (vi) in terms of the nonspherical stellar distribution, the jet interaction with the surrounding gas could also be revealed via the nonisotropic distribution of ionization tracers. In particular, the shock-tracer line [Fe III] seems to be preferentially located in the direction of the mini cavity (Peißker et al. 2020), which suggests either current or past interaction of the gas with the high-velocity outflow/jet (Yusef-Zadeh et al. 2020). On scales larger than 1 pc, the nonisotropic distribution is manifested by bipolar radio lobes (Heywood et al. 2019) and X-ray (Ponti et al. 2019) and γ-ray bubbles (Su et al. 2010; Ackermann et al. 2014). Recently, the analysis of the tilted, partially ionized disk in the inner Galactic latitudes has shown that its optical line ratios are characteristic of low-ionization nuclear emission regions (LINERs; Krishnarao et al. 2020). The bipolar ionization structure is energetically in favor of the Seyfert-like jet activity rather

than the star formation event (Bland-Hawthorn et al. 2019).

In summary, the jet-activity signs listed in points (i)–(vii) indicated the past enhanced activity of the jet and its interaction with the surrounding circumnuclear medium, including the nuclear star cluster. Although each of the above-mentioned points can have alternative explanations, the absence of all of these signatures would suggest that the jet did not operate in the past, and our hypotheses would then be strongly disfavored. Future detailed observations by the Extremely Large Telescope (ELT) in combination with detailed numerical simulations of the jet–star interactions close to Sgr A* will help to reveal the signatures of current and past jet–star interactions.

7. Summary and Conclusions

We presented a novel scenario to explain the lack of bright red giants in the inner regions of the Galactic center in the sphere of influence of the currently quiescent, but previously active, radio source Sgr A*. Taking this increased activity into account, we focused on the effect of the jet on late-type stars at $\lesssim$0.3 pc. By adopting the scenario of the recent active period of Sgr A*, we considered the interaction of red giants with a jet of a typical active Seyfert-like nucleus with the expected kinetic luminosity $L_{\rm j} = 10^{41}$–10^{44} erg s^{-1}. Given that red giants have a very slow wind, the jet can significantly ablate the stellar envelope down to at least $\sim 30\,R_\odot$ within the S cluster ($z \lesssim 0.04$ pc) after repetitive encounters. Specifically, at $z = 0.02$ pc, the stagnation radius is $4 \leqslant R_{\rm stag}/R_\odot \leqslant 30$ for $2.0 \times 10^{41} \leqslant L_{\rm j}/{\rm erg\ s^{-1}} \leqslant 1.1 \times 10^{43}$. Hence, the higher luminosity end that corresponds to the less frequent events that formed the Fermi bubbles can ablate the stellar atmospheres of late-type giants by a factor of $\sim$7.5 more than the more frequent, less energetic outbursts of Sgr A*.

This truncation is accompanied by the removal of a large fraction of matter, reaching as much as $\Delta M_1 \approx 3 \times 10^{-5}\,M_\odot \approx 10 M_{\rm Earth}$ for red giants with radii $R_\star > 200\,R_\odot$ at distances smaller than 0.01 pc for a single encounter. After at least a thousand red giant–jet encounters, we expect the cumulative mass loss of at least $\Delta M \approx 10^{-4}\,M_\odot$ at the orbital distance of 0.01 pc. This is comparable to the values inferred from red giant–accretion-clump simulations. The proposed mechanism can thus help to explain the presence of late-type stars with the maximum atmosphere radius of $\sim 30 R_\odot$ within the S cluster as inferred from the near-infrared observations.

The reduction in the mass and radius of the red giant atmosphere after repetitive jet–star crossings will produce an estimated decrease in the near-infrared K-band magnitude by 1.9, 5.3, and 8.9 mag with respect to the normal evolution at 0.1, 0.01, and 0.001 pc from Sgr A*, respectively. Simultaneously, the color index would decrease to negative values, i.e., the stars should appear bluer with a higher effective temperature. The mean expected number of red giant–jet crossings per orbital period is 3.5 within 0.04 pc, and 82.5 within 0.3 pc, respectively. For the jet kinetic luminosity of 10^{44} erg s^{-1}, $\sim$26.5% of currently detectable late-type stars located at $z = 0.04$ pc (S cluster) with radii larger than $2.7\,R_\odot$ and K-band magnitudes smaller than $\sim$16 mag could be affected by the jet ablation. The estimated numbers of interacting giants can be considered as lower limits because various dynamical effects, such as the coherent resonant relaxation within the nuclear star cluster as well as a potential jet precession would enlarge the number of affected giants.

Constructed surface-brightness profiles of the mock NSC affected by the jet with the luminosity of 10^{42}–10^{44} erg s^{-1} show that profiles of mainly brighter late-type stars with $m_K < 14$ mag (dereddened, <16 mag with the foreground extinction included) are flattened by the jet inside the inner arcsecond ($\lesssim$0.04 pc). Fainter stars keep the initially assumed cusp-like projected profile.

In summary, the interaction of red giants with the jet of Sgr A* during its enhanced activity could contribute to the observed lack of bright red giants and hence affect their surface-brightness profile in the central parts of the NSC. More likely, this mechanism operated in parallel with other previously proposed mechanisms, such as the star–disk interactions, star–star collisions, and TDEs that have different spatial scales of efficiency. Detailed numerical computations of red giant–jet interactions in combination with a modified stellar evolution will help to verify our analytical estimates.

We thank the referee for constructive comments that helped us improve our manuscript. M.Z., B.C., and V.K. acknowledge the continued support by the National Science Center, Poland, grant No. 2017/26/A/ST9/00756 (Maestro 9), and the Czech-Polish mobility program (MSMT 8J20PL037). A.A. and V.K. acknowledge the Czech Science Foundation under grant GACR 20-19854S titled "Particle Acceleration Studies in Astrophysical Jets," and the European Space Agency PRODEX project eXTP in the Czech Republic. This work was carried out partly also within the Collaborative Research Center 956, subproject [A02], funded by the Deutsche Forschungsgemeinschaft (DFG) project ID184018867. The work on this project was partially carried out during the short-term stay of M.Z. within the Polish-Czech bilateral exchange program supported by NAWA under agreement PPN/BCZ/2019/1/00069. M.Z. also acknowledges the NAWA financial support under agreement PPN/WYM/2019/1/00064 to perform a three-month exchange stay at the Astronomical Institute of the Czech Academy of Sciences in Prague.

ORCID iDs

Michal Zajaček https://orcid.org/0000-0001-6450-1187
Anabella Araudo https://orcid.org/0000-0001-7605-5786
Vladimír Karas https://orcid.org/0000-0002-5760-0459
Bożena Czerny https://orcid.org/0000-0001-5848-4333
Andreas Eckart https://orcid.org/0000-0001-6049-3132

References

Abraham, Z., & Carrara, E. A. 1998, ApJ, 496, 172
Ackermann, M., Albert, A., Atwood, W. B., et al. 2014, ApJ, 793, 64
Alexander, T. 2005, PhR, 419, 65
Alexander, T. 2017, ARA&A, 55, 17
Ali, B., Paul, D., Eckart, A., et al. 2020, ApJ, 896, 100
Amaro-Seoane, P., & Chen, X. 2014, ApJL, 781, L18
Amaro-Seoane, P., Chen, X., Schödel, R., & Casanellas, J. 2020, MNRAS, 492, 250
Antonini, F., Capuzzo-Dolcetta, R., Mastrobuono-Battisti, A., & Merritt, D. 2012, ApJ, 750, 111
Araudo, A. T., Bosch-Ramon, V., & Romero, G. E. 2013, MNRAS, 436, 3626
Araudo, A. T., & Karas, V. 2017, in Proc. RAGtime 17–19: Workshops on Black Holes and Neutron Stars (Opava: Silesian Univ.), 1
Armitage, P. J., Zurek, W. H., & Davies, M. B. 1996, ApJ, 470, 237
Baganoff, F. K., Maeda, Y., Morris, M., et al. 2003, ApJ, 591, 891
Bailey, V. C., & Davies, M. B. 1999, MNRAS, 308, 257
Barkov, M. V., Aharonian, F. A., Bogovalov, S. V., Kelner, S. R., & Khangulyan, D. 2012a, ApJ, 749, 119
Barkov, M. V., Aharonian, F. A., & Bosch-Ramon, V. 2010, ApJ, 724, 1517

Barkov, M. V., Bosch-Ramon, V., & Aharonian, F. A. 2012b, ApJ, 755, 170
Baumgardt, H., Gualandris, A., & Portegies Zwart, S. 2006, MNRAS, 372, 174
Bednarek, W., & Banasiński, P. 2015, ApJ, 807, 168
Bell, A. R. 1978, MNRAS, 182, 147
Blandford, R. D., & Payne, D. G. 1982, MNRAS, 199, 883
Bland-Hawthorn, J., & Cohen, M. 2003, ApJ, 582, 246
Bland-Hawthorn, J., Maloney, P. R., Sutherland, R., et al. 2019, ApJ, 886, 45
Boehle, A., Ghez, A. M., Schödel, R., et al. 2016, ApJ, 830, 17
Bogdanović, T., Cheng, R. M., & Amaro-Seoane, P. 2014, ApJ, 788, 99
Bosch-Ramon, V., Perucho, M., & Barkov, M. V. 2012, A&A, 539, A69
Bressan, A., Marigo, P., Girardi, L., et al. 2012, MNRAS, 427, 127
Britzen, S., Fendt, C., Böttcher, M., et al. 2019a, A&A, 630, A103
Britzen, S., Fendt, C., Witzel, G., et al. 2018, MNRAS, 478, 3199
Britzen, S., Fendt, C., Zajaček, M., et al. 2019b, Galax, 7, 72
Buchholz, R. M., Schödel, R., & Eckart, A. 2009, A&A, 499, 483
Czerny, B., Kunneriath, D., Karas, V., & Das, T. K. 2013, A&A, 555, A97
Dale, J. E., Davies, M. B., Church, R. P., & Freitag, M. 2009, MNRAS, 393, 1016
Davies, M. B., & King, A. 2005, ApJL, 624, L25
de la Cita, V. M., Bosch-Ramon, V., Paredes-Fortuny, X., Khangulyan, D., & Perucho, M. 2016, A&A, 591, A15
Deegan, P., & Nayakshin, S. 2007, MNRAS, 377, 897
Dexter, J., & Fragile, P. C. 2013, MNRAS, 432, 2252
Do, T., Ghez, A. M., Morris, M. R., et al. 2009, ApJ, 703, 1323
Do, T., Kerzendorf, W., Konopacky, Q., et al. 2018, ApJL, 855, L5
Eckart, A., Hüttemann, A., Kiefer, C., et al. 2017, FoPh, 47, 553
Ernst, A., Just, A., & Spurzem, R. 2009, MNRAS, 399, 141
Gallego-Cano, E., Schödel, R., Dong, H., et al. 2018, A&A, 609, A26
Genzel, R., Eisenhauer, F., & Gillessen, S. 2010, RvMP, 82, 3121
Genzel, R., Thatte, N., Krabbe, A., Kroker, H., & Tacconi-Garman, L. E. 1996, ApJ, 472, 153
Ghez, A. M., Duchêne, G., Matthews, K., et al. 2003, ApJL, 586, L127
Gillessen, S., Plewa, P. M., Eisenhauer, F., et al. 2017, ApJ, 837, 30
Gravity Collaboration, Abuter, R., Amorim, A., et al. 2018, A&A, 615, L15
Gualandris, A., & Merritt, D. 2012, ApJ, 744, 74
Guo, F., & Mathews, W. G. 2012, ApJ, 756, 181
Habibi, M., Gillessen, S., Martins, F., et al. 2017, ApJ, 847, 120
Habibi, M., Gillessen, S., Pfuhl, O., et al. 2019, ApJL, 872, L15
Heywood, I., Camilo, F., Cotton, W. D., et al. 2019, Natur, 573, 235
Hills, J. G. 1975, Natur, 254, 295
Ito, H., Kino, M., Kawakatu, N., Isobe, N., & Yamada, S. 2008, ApJ, 685, 828
Joss, P. C., Rappaport, S., & Lewis, W. 1987, ApJ, 319, 180
Junor, W., Biretta, J. A., & Livio, M. 1999, Natur, 401, 891
Karas, V., & Šubr, L. 2001, A&A, 376, 686
Kieffer, T. F., & Bogdanović, T. 2016, ApJ, 823, 155
Kim, S. S., & Morris, M. 2003, ApJ, 597, 312
King, A. 2020, MNRAS, 493, L120
Komissarov, S. S. 1994, MNRAS, 269, 394
Komossa, S. 2015, JHEAp, 7, 148
Krabbe, A., Genzel, R., Drapatz, S., & Rotaciuc, V. 1991, ApJL, 382, L19
Krishnarao, D., Benjamin, R. A., & Haffner, L. M. 2020, SciA, 6, 9711
Kroupa, P. 2001, MNRAS, 322, 231
Levin, Y., & Beloborodov, A. M. 2003, ApJL, 590, L33
Li, Z., Morris, M. R., & Baganoff, F. K. 2013, ApJ, 779, 154
Löckmann, U., & Baumgardt, H. 2008, MNRAS, 384, 323
Lodato, G., & Pringle, J. E. 2006, MNRAS, 368, 1196
MacLeod, M., Guillochon, J., & Ramirez-Ruiz, E. 2012, ApJ, 757, 134
MacLeod, M., & Lin, D. N. C. 2020, ApJ, 889, 94
Madigan, A.-M., Hopman, C., & Levin, Y. 2011, ApJ, 738, 99
Mapelli, M., & Gualandris, A. 2016, in Star Formation and Dynamics in the Galactic Centre, ed. F. Haardt et al., Vol. 905 (Berlin: Springer)
Matsubayashi, T., Makino, J., & Ebisuzaki, T. 2007, ApJ, 656, 879
Merritt, D. 2013, Dynamics and Evolution of Galactic Nuclei (Princeton, NJ: Princeton Univ. Press)
Merritt, D., & Szell, A. 2006, ApJ, 648, 890
Miller, M. J., & Bregman, J. N. 2016, ApJ, 829, 9
Miller-Jones, J. C. A., Tetarenko, A. J., Sivakoff, G. R., et al. 2019, Natur, 569, 374
Milosavljević, M., & Loeb, A. 2004, ApJL, 604, L45
Monceau-Baroux, R., Porth, O., Meliani, Z., & Keppens, R. 2015, A&A, 574, A143
Morel, P., & Lebreton, Y. 2008, Ap&SS, 316, 61
Morris, M. 1993, ApJ, 408, 496
Morris, M., & Serabyn, E. 1996, ARA&A, 34, 645
Moser, L., Sánchez-Monge, Á., Eckart, A., et al. 2017, A&A, 603, A68
Mužić, K., Eckart, A., Schödel, R., et al. 2010, A&A, 521, A13
Paczyński, B. 1970, AcA, 20, 47
Parsa, M., Eckart, A., Shahzamanian, B., et al. 2017, ApJ, 845, 22
Peißker, F., Hosseini, S. E., Zajaček, M., et al. 2020, A&A, 634, A35
Peißker, F., Zajaček, M., Eckart, A., et al. 2019, A&A, 624, A97
Perez, K., Hailey, C. J., Bauer, F. E., et al. 2015, Natur, 520, 646
Perucho, M., Bosch-Ramon, V., & Barkov, M. V. 2017, A&A, 606, A40
Pfuhl, O., Fritz, T. K., Zilka, M., et al. 2011, ApJ, 741, 108
Phinney, E. S. 1989, in IAU Symp. 136, The Center of the Galaxy, ed. M. Morris (Dordrecht: Kluwer), 543
Ponti, G., Hofmann, F., Churazov, E., et al. 2019, Natur, 567, 347
Portegies Zwart, S. F., Baumgardt, H., McMillan, S. L. W., et al. 2006, ApJ, 641, 319
Rees, M. J. 1988, Natur, 333, 523
Refsdal, S., & Weigert, A. 1971, A&A, 13, 367
Reimers, D. 1987, in IAU Symp. 122, Circumstellar Matter, ed. I. Appenzeller & C. Jordan (Dordrecht: Reidel), 307
Różańska, A., Kunneriath, D., Czerny, B., Adhikari, T. P., & Karas, V. 2017, MNRAS, 464, 2090
Schödel, R., Feldmeier, A., Neumayer, N., Meyer, L., & Yelda, S. 2014, CQGra, 31, 244007
Schödel, R., Najarro, F., Muzic, K., & Eckart, A. 2010, A&A, 511, A18
Schödel, R., Nogueras-Lara, F., Gallego-Cano, E., et al. 2020, A&A, 641, A102
Sellgren, K., McGinn, M. T., Becklin, E. E., & Hall, D. N. 1990, ApJ, 359, 112
Su, M., Slatyer, T. R., & Finkbeiner, D. P. 2010, ApJ, 724, 1044
Šubr, L., & Haas, J. 2014, ApJ, 786, 121
Sunyaev, R., & Churazov, E. 1998, MNRAS, 297, 1279
Sunyaev, R. A., Markevitch, M., & Pavlinsky, M. 1993, ApJ, 407, 606
Syer, D., & Ulmer, A. 1999, MNRAS, 306, 35
Vilkoviskij, E. Y., & Czerny, B. 2002, A&A, 387, 804
Wang, Q. D., Nowak, M. A., Markoff, S. B., et al. 2013, Sci, 341, 981
Yusef-Zadeh, F., Arendt, R., Bushouse, H., et al. 2012, ApJL, 758, L11
Yusef-Zadeh, F., Royster, M., Wardle, M., et al. 2020, MNRAS, 499, 3909
Zhao, J.-H., Morris, M. R., Goss, W. M., & An, T. 2009, ApJ, 699, 186
Zhu, Z., Li, Z., & Morris, M. R. 2018, ApJS, 235, 26
Zurek, W. H., Siemiginowska, A., & Colgate, S. A. 1994, ApJ, 434, 46